Upper mantle mush zones beneath low melt flux ocean island volcanoes: insights from Isla Floreana, Galápagos

Matthew L. M. Gleeson[1]*, Sally A. Gibson[1] and Michael J. Stock[1,2]
[1]Department of Earth Sciences, University of Cambridge, Downing Street, CB2 3EQ, UK
[2]Department of Geology, Trinity College Dublin, College Green, Dublin 2, Ireland.
*Corresponding author email address: mlmg3@cam.ac.uk

ABSTRACT

The physicochemical characteristics of sub-volcanic magma storage regions have important implications for magma system dynamics and pre-eruptive behaviour. The architecture of magma storage regions located directly above high buoyancy flux mantle plumes (such as Kīlauea, Hawaii and Fernandina, Galápagos) are relatively well understood. However, far fewer constraints exist on the nature of magma storage beneath ocean island volcanoes that are distal to the main zone of mantle upwelling or above low buoyancy flux plumes, despite these systems representing a substantial proportion of global ocean island volcanism. To address this, we present a detailed petrological study of Isla Floreana in the Galápagos Archipelago, which is characterised by an extremely low flux of magma into the lithosphere from the underlying mantle plume. Detailed *in situ* major and trace element analyses of crystal phases within exhumed cumulate xenoliths, lavas and scoria deposits, indicate that magma storage beneath Floreana is dominated by crystal-rich domains (i.e. mush). Trace element disequilibria between cumulus phases and erupted melts, as well as trace element zoning within the xenolithic clinopyroxenes, reveals that reactive porous flow (previously identified beneath mid-ocean ridges) is an important process of melt transport within these crystal-rich storage regions. In addition, application of three petrological barometers reveal that the Floreana mush zones are located in the upper mantle, at a depth of 23.7±5.1 km. Our barometric results are compared to recent studies of high melt flux volcanoes in the western Galápagos, Hawaii and Iceland, and demonstrate that the flux of magma from the underlying mantle source represents a first-order control on the depth and physical characteristics of magma storage beneath ocean island volcanoes.

KEY WORDS

Galápagos; magma storage; reactive porous flow; barometry.

1 INTRODUCTION

The physicochemical characteristics (such as size, pressure, volatile content and geochemical heterogeneity) of magma storage at volcanic centres located directly above high buoyancy flux mantle plumes (e.g. Kīlauea, Hawaii and Isabela, Galápagos) have been subject to intense study over the past few decades (Bagnardi et al., 2013; Clague and Denlinger, 1994; Geist et al., 1998; Naumann and Geist, 1999; Park et al., 2007; Pietruszka et al., 2015; Poland et al., 2015; Stock et al., 2018; Wieser et al., 2020, 2019). Systems such as Kīlauea are characterised by frequent volcanic activity, and geophysical (seismicity, ground deformation) and geochemical (gas emissions) monitoring is prevalent. Monitoring data, combined with petrological and geochemical analysis of erupted products (mineral textures, deformation characteristics and chemistry) provide important insights into the architecture and dynamics of their sub-volcanic plumbing systems (Amelung et al., 2000; Davidge et al., 2017; Geist et al., 2014; Hartley et al., 2018; Kilbride et al., 2016). However, these systems (which we term 'high melt flux') represent only one endmember of global plume-derived volcanism. Low melt flux systems, either above low buoyancy flux plumes (e.g. Canary Islands; Longpre et al., 2014) or at volcanic systems distal to the centre of mantle melting at high buoyancy flux mantle plumes (e.g. eastern and southern Galápagos; Harpp and Geist, 2018), are the other endmember.

Although a substantial number of Holocene hotspot-related volcanic systems are located in regions characterised by a relatively low flux of magma into the lithosphere (e.g. Samoa, Canary Islands, Cape Verde; Global Volcanism Program, 2013), only a small number of eruptions have been observed (and recorded) at these systems since the advent of modern volcano monitoring techniques. As a result, few constraints exist on the conditions of magma storage in regions characterised by a low flux of magma into the lithosphere, relative to volcanic centres located above the centre of mantle plumes with a large buoyancy flux (and thus generating a large flux of magma). The flux of mantle-derived magma into the lithosphere is important because it is thought to impart a first-order control on the development of large silicic magma bodies (Barker et al., 2020) and the homogeneity of erupted

liquids (Geist et al., 2014). Furthermore, placing constraints on the physicochemical characteristics of magma storage at low melt flux ocean island volcanoes is essential for determining the influence of mantle dynamics and melt generation processes on the structure and physical characteristics of sub-volcanic magma plumbing systems. In the absence of detailed monitoring data, petrological and geochemical analyses of volcanic products from past eruptions represent the only available tools for determining the structure and processes operating within these systems.

Isla Floreana in the south-eastern Galápagos Archipelago is currently located ~100 km downstream from where the Galápagos plume impacts on the base of the lithosphere beneath the island of Isabela in the western archipelago (Fig. 1; Villagómez et al., 2014). Hence, although the Galápagos plume has a relatively high buoyancy flux (compared to regions such as the Canary Islands; Jackson et al., 2017), Floreana's location relative to the main zone of mantle plume upwelling results in an extremely low flux of magma entering the lithosphere and, consequently, very infrequent volcanic activity (Harpp et al., 2014a; Harpp and Geist, 2018). In this paper, we present a thorough petrological study of scoria, lava and xenolith samples from Floreana and place constraints of the structure, depth and crystallinity of magmatic systems beneath this low melt flux ocean island volcano. We compare our results with more frequently active volcanic centres in the western Galápagos (near the centre of plume upwelling; Geist et al., 1998; Naumann and Geist, 1999; Stock et al., 2018), as well as Iceland and Hawaii (Hammer et al., 2016; Hartley et al., 2018; Poland et al., 2015), to investigate how the flux of magma into the lithosphere influences the depth and crystallinity of sub-volcanic magma storage regions.

2 GEOLOGICAL BACKGROUND

The Galápagos Archipelago in the eastern equatorial Pacific is one of the most volcanically active regions on Earth, with eruptions typically occurring every 2–3 years (Global Volcanism Program, 2013). Although most historic Galápagos eruptions have taken place on the two westernmost islands of Isabela and Fernandina (Fig. 1), infrequent volcanic activity has also occurred on several islands in

the eastern and southern Galápagos (e.g. Santiago in 1906 and Marchena in 1991; Global Volcanism Program, 2013).

Volcanoes in the western Galápagos likely emerged within the last 500 kyr (Naumann and Geist, 2000), whereas those in the eastern and south-eastern Galápagos are considerably older (eruption ages up to 2.3 Ma and 3.2 Ma have been measured on San Cristobal and Espanola, respectively; Bailey, 1976; Geist et al., 1986). In addition, substantial differences in geomorphology and the style of volcanic activity are observed across the archipelago (Geist et al., 1995; Harpp et al., 2014a; Harpp and Geist, 2018). For example, volcanoes in the western archipelago are typified by large summit calderas (<700m deep), which are not present on the eastern islands (Chadwick and Howard, 1991; Cleary et al., 2020; Harpp and Geist, 2018).

Geochemical distinctions between the western and eastern/southern Galápagos islands are also observed, which are primarily related to variations in the composition of the underlying mantle source (Geist et al., 1988; Gibson and Geist, 2010; Gleeson et al., 2020; Harpp and White, 2001; White et al., 1993) or the volume flux of mantle-derived magma that ascends into the lithosphere (Geist et al., 1995, 2014; Gibson et al., 2016; Harpp and Geist, 2018). For example, variations in the flux of mantle derived magma are hypothesised to influence the geochemical heterogeneity of erupted basalts at each island: volcanoes in the western archipelago typically erupt a very narrow range of basaltic compositions over hundreds of millennia during their main shield building phase, whereas basalts erupted from a single island in the eastern and/or south-eastern archipelago, such as Floreana, tend to display far greater compositional heterogeneity (Geist et al., 2014; Harpp and Geist, 2018).

Floreana is characterised by numerous scoria cones (up to ~600m elevation at Cerro Pajas) and blocky, heavily vegetated lava flows that can typically be traced to the cone from which they originated (Harpp et al., 2014a). The crustal thickness beneath Floreana is ~16 km, similar to that observed in the western Galápagos 10–18 km (Feighner and Richards, 1994), and the lithospheric thickness beneath the western and south-eastern Galápagos is very similar (~50–60 km; Gibson and Geist, 2010). However, recent work has shown that the volumetric eruption rate on Floreana is 1–10 $m^3 \cdot yr^{-1}$ over the past 1–1.5 Myrs, millions of times lower than the current effusion rate at volcanoes in

the western Galápagos (cf. ~$4.4 \cdot 10^6$ $m^3 \cdot yr^{-1}$ at Fernandina; Harpp et al., 2014a; Kurz et al., 2014). This variation in volumetric eruption rate likely reflects a substantially lower flux of magma into the lithosphere beneath Floreana than beneath each volcanic centre in the western Galápagos. Additionally, Floreana has a high proportion of pyroclastic deposits compared to the other Galápagos islands (Harpp et al., 2014a) and eruption deposits typically contain a large number of cumulate xenoliths (Lyons et al., 2007). The abundance of pyroclastic deposits and xenoliths on Floreana has been interpreted as evidence for very high magma ascent rates (Harpp et al., 2014a).

Floreana is one of the only Galápagos islands that displays evidence for multiple stages in its volcanic evolution. Submarine parts of the island have isotopic and trace element characteristics that are similar to recent basalts erupted on southern Isabela (e.g. Sierra Negra and Cerro Azul, Fig. 1A), whereas the subaerial material is isotopically distinct (high $^{206}Pb/^{204}Pb$ ratios; Harpp et al., 2014). The trace element and isotopic variation in the erupted basalts is mirrored in xenoliths found in the Floreana lava and scoria deposits: gabbroic xenoliths have radiogenic isotope ratios that are similar to modern Isabela basalts, whereas wehrlitic xenoliths have trace element and isotopic compositions that resemble recent Floreana subaerial basalts (Lyons et al., 2007). Variations in the isotopic characteristics of the Floreana lavas (submarine vs subaerial) and xenoliths (gabbros vs wehrlites) are thought to indicate a change in the mean composition of magma produced by mantle melting beneath the island at ~1–1.5 Ma (Harpp et al., 2014a). In this study, we focus on constraining the depth and physical characteristics of magma storage during the most recent period of volcanic activity on Isla Floreana (<1–1.5 Ma) using chemical and textural analysis of crystal phases in lava flows and xenolithic nodules.

3 SAMPLES AND PETROGRAPHY

The Floreana samples analysed in this study were collected during a field campaign to the northern part of the island in June 2017 and consist of lavas (27 samples), scoria (2 samples) and xenoliths (4 wehrlite, 3 dunite and 2 gabbro samples; Fig. 1B). Most lava samples were collected from the unaltered, low vesicularity cores of blocky flows or glassy flow fronts. The scoria samples were

collected from two separate deposits and comprise rapidly cooled tephra fragments (~0.5–2 cm across; 17MMSG16) and scoria bombs (~10 cm across; 17MMSG20). Xenolithic fragments (3–15cm across) were sampled from two different scoria cones on the north-east coast of Floreana and are also found within most lava flows across the entire island (Fig. 1).

3.1 Lavas and scoria

The lava and scoria samples analysed in this study are typically olivine phyric with minor andehral clinopyroxene and very rare orthopyroxene. Except for small plagioclase laths in the microcrystalline groundmass, plagioclase crystals are extremely rare in Floreana lavas. Plagioclase macrocrysts are only present in one of our lava samples (17MMSG29) where they occur as isolated phenocrysts and in plagioclase-olivine crystal clots (Table S.1). Abundant olivine and the absence of plagioclase in the Floreana lavas and scoria contrasts with basalts in the central, northern, and western parts of the Galápagos Archipelago, where plagioclase-phyric and ultraphyric basalts are common (Geist et al., 2002; Gibson et al., 2012; Harpp et al., 2014b).

Despite their relatively simple mineralogy, Floreana lava and scoria samples contain texturally diverse olivine crystals which can be divided into five distinct groups (Fig. 2):

- Group 1 olivines are present in all lava and scoria samples and are the most abundant type of olivine found in the Floreana basalts (~60-70% of all crystals). They are characterised by homogeneous cores and narrow normally zoned rims (Fig. 2A). Group 1 olivines are generally subhedral to euhedral.
- Group 2 olivines are the second most abundant group in the Floreana lava and scoria deposits (~20-30%) and display reverse zoning patterns. They are typically euhedral, with occasional small embayments (Fig. 2B).
- Group 3 olivines are also reversely zoned, but are distinguished by skeletal overgrowths, indicating significant undercooling of the host magma and rapid crystal growth (Fig. 2C; Donaldson, 1976; Welsch et al., 2014). Group 3 olivines are less abundant than Groups 1 and 2 olivines in Floreana lava and scoria deposits (<10%).

- Group 4 olivines are present in low abundance in the Floreana lava and scoria deposits (<10%). They have homogeneous cores and reverse-zoned rims (up to ~300 μm thick). The rims have sieve textures, indicating resorption and chemical disequilibrium with their carrier melts (Fig. 2D).
- Group 5 olivines are only found in a minority of samples and are characterised by the presence of 4 compositional zones with alternating high and low forsterite contents (visible in back-scattered electron images; Fig. 2E and F).

3.2 Xenoliths

3.2.1 Gabbroic xenoliths

Floreana gabbroic xenoliths predominantly comprise plagioclase (33–66 vol.%), clinopyroxene (28–46 vol.%) and orthopyroxene (5–15 vol.%), with little or no olivine (Table S.2). Plagioclase and pyroxene crystals are typically >500 μm and grain sizes are relatively constant within a single xenolith sample. Where three plagioclase grains meet at a triple junction, 120° grain boundaries indicate a high degree of textural equilibrium (Fig. 3A; Holness et al., 2005). Some of the gabbros display clear clinopyroxene-rich and plagioclase-rich layers (2–5 mm), whereas others have a more irregular mineral distribution.

3.2.2 Dunitic xenoliths

Cumulus olivine dominates dunitic Floreana xenoliths (>90 vol.%). The olivine crystals are subhedral to euhedral and may have undergone partial textural re-equilibration, with some olivine triple junctions approaching 120° grain boundaries. Minor intercumulus clinopyroxene is present along grain boundaries and between pre-existing olivine crystals (Fig. 3B).

3.2.3 Wehrlitic xenoliths

Floreana wehrlitic xenoliths contain olivine (>50 vol.%), clinopyroxene (20–40 vol.%), orthopyroxene (~0–7 vol.%) and minor spinel (<1 vol.%; Table S.1). Clinopyroxene typically occurs as large (<5 mm) oikocrysts, which enclose rounded olivine chadacrysts (<500 μm in diameter and separated by distances of <400 μm; Fig. 2C and D). In the most pyroxene-rich samples (e.g. 17MMSG03a), clinopyroxene crystals contain fine-scale orthopyroxene exsolution lamallae (Fig. 2E

and F). Olivine grains that are not enclosed by clinopyroxene are typically larger (>1 mm) and more euhedral than the chadacrysts. In some samples, the boundary between clinopyroxene and olivine crystals is characterised by a thin (<20-30 μm) layer of glass and very fine-grained microcrysts. Orthopyroxene is an intercumulus phase in the wehrlitic xenoliths and has an anhedral morphology, infilling the space between earlier formed clinopyroxene and olivine grains. Our observations of dunitic and wehrlitic xenoliths (which have the isotopic signatures of modern day Floreana basalts; Lyons et al., 2007) indicate that the typical order of crystallisation beneath Floreana is olivine, followed by clinopyroxene, with little to no crystallisation of plagioclase.

4 ANALYTICAL METHODOLOGY

4.1 Electron microprobe analysis

Glass chips, olivine and clinopyroxene crystals were hand-picked from crushed scoria and lava samples, mounted in epoxy or indium, and then ground and polished prior to analysis (crystals mounted in indium were polished individually prior to mounting). Xenolithic crystals were analysed as individual crystals mounted in indium or *in situ* in petrographic thin sections. The major and minor element concentrations of olivine, clinopyroxene and glass were measured using a Cameca SX100 electron microprobe in the Department of Earth Sciences, University of Cambridge. Calibrations were made using mineral and metal standards prior to each analytical session (see Gleeson and Gibson, 2019 for details). Glasses in the two Floreana scoria samples were analysed using a 6 nA, 15 kV, defocused (5 μm) beam for most elements. Na and K were analysed first (10 s peak count time) to avoid alkali migration. Other elements were analysed with peak count times of 10 s (Si), 20 s (Fe), 30 s (Al, P, Ca, Mg), 40 s (Mn), or 60 s (Ti). Sulphur was analysed last using a 20 nA beam current and a 60 s peak count time.

Pyroxene compositions were determined by spot analyses using a 20 nA, 15 kV, focused (~1 μm) beam, with Na, K and Si analysed first (10 s). Element maps of Cr, Ti, and Al in key clinopyroxene crystals from the Floreana xenoliths were created using a 60 nA, 15 kV, focused (~1 μm) beam, with a dwell time of 150 ms. Cr counts were collected on a PET and a LIF crystal, Al counts were

collected on two TAP crystals, and Ti counts were collected on a PET crystal. Olivine electron microprobe analysis was carried out using the method outlined in Gleeson and Gibson (2019).

Analytical uncertainties were tracked through analysis of appropriate Smithsonian Microbeam Standards (Jarosewich et al., 1980). Accuracy is typically between 98 and 102% for all phases. 2σ analytical precision of clinopyroxene and olivine analysis is typically better than 2–3% for major elements (>1 wt%) and typically ~5-10% for minor elements (<1 wt%). Similarly, the 2σ precision for glass analysis is typically <3% for major elements, ~5% for Na, and ~10% for K (See Supplementary File).

4.2 Laser ablation Inductively Coupled Plasma Mass Spectrometry

Trace element concentrations were measured in the apparent cores (i.e. as exposed in the 2D plane) of clinopyroxene crystals from scoria and xenolith samples using an ESI193 laser coupled to a Nexion 350D inductively coupled plasma mass spectrometer in the Department of Earth Sciences, University of Cambridge. Analyses were collected in spot mode using a 20 Hz laser repetition rate, 4 J/cm^2 fluence and 80 μm spot size, or in transect mode using a 10 Hz repetition rate, 3.5 J/cm^2 fluence and 30 μm spot size. For transects, individual spots were offset into two (alternating) lines to increase the spatial resolution. Laser ablation inductively coupled plasma mass spectrometry (LA-ICP-MS) data reduction was carried out in Iolite©, with NIST 612SRM as the standard reference material and Ca (from electron microprobe analysis) as the internal reference standard. Analytical accuracy was tracked using a USGS glass standard (Jochum et al., 2016) and is between 95% and 105% for most elements (See Supplementary File). 2σ analytical precision of spot analyses was monitored through analysis of an in-house clinopyroxene standard and is 5–10% for the light rare-earth elements (LREE), Y, Sr, and Zr and 10–20% for the heavy rare earth element (HREE). 2σ analytical precision is ~10% for all elements of interest (Ce, Y) in transect analyses.

5 GLASS AND MINERAL CHEMISTRY

5.1 Matrix glass compositions

The matrix glass compositions measured in one scoria (17MMSG16) and one glassy lava sample (17MMSG12) from Floreana have very similar MgO concentrations (6.06–6.36 wt%) but exhibit differences in the concentrations of other elements (Fig. 4). For example, sample 17MMSG12 has consistently lower TiO_2 and Al_2O_3 concentrations than 17MMSG16, which must either reflect heterogeneity in the composition of primary mantle melts or variations in crustal processing (e.g. the extent of plagioclase or clinopyroxene crystallisation; Fig. 4). Differences between our matrix glass major element analyses and previously-published whole-rock data from Floreana (Harpp et al., 2014a) are primarily due to olivine accumulation in the whole-rock samples (additional accumulation of clinopyroxene may explain the high CaO content of some whole-rock samples; Fig. 4C).

Our Floreana matrix glass analyses have higher Al_2O_3 concentrations than basaltic glass and whole-rock measurements from the western Galápagos Archipelago (excluding whole-rock samples with accumulated plagioclase, Fig. 4D; Geist et al., 2002). This indicates substantially lower extents of plagioclase fractionation in the Floreana magmatic system and is consistent with the scarcity of plagioclase phenocrysts in erupted Floreana lavas. Reduced plagioclase crystallisation could be due to the major element composition or H_2O content of primary mantle melts and/or the increased pressure of magma storage (Asimow and Langmuir, 2003; Neave et al., 2019; Thompson, 1987; Winpenny and Maclennan, 2011).

5.2 Olivine compositions

Olivine crystals in our Floreana lava and scoria samples show large variations in their forsterite contents (Fo = 70–92, where Fo=(Mg/(Mg+Fe^{2+}) molar) with histograms showing a primary density peak at Fo~85 (Fig. 5), more primitive than the olivine composition in equilibrium with basaltic glasses from Floreana (K_D = 0.30; Roeder and Emslie, 1970). Although there is no clear correlation between Fo and Ca concentration in these crystals, the most forsteritic olivines (Fo>83) have

extremely diverse Ca contents (~250 to ~2600 ppm; Fig. 5), whereas crystals with lower Fo contents (<83) have ubiquitously low Ca concentrations (<1500 ppm). Floreana olivines separated from the lava and scoria samples also have a large range of Ni concentrations (~700 to ~3200 ppm), consistent with crystallisation from a peridotite-derived melt (Fig. 5; Gleeson and Gibson, 2019; Herzberg, 2011; Matzen et al., 2017b, 2017a). All olivine crystals analysed in the wehrlite and dunite xenoliths have a narrow range of Fo contents (83-87) and, crucially, have uniformly low Ca concentrations (<1000 ppm) and moderately high Ni contents (~2000 ppm). The range in Ca contents contrasts with olivines from other Galápagos islands where Ca is typically >1000 ppm (Gleeson and Gibson, 2019; Vidito et al., 2013). The Ca and Ni contents of our Floreana olivines are inversely related at a set Fo content (Fig. 5).

5.3 Clinopyroxene compositions

5.3.1 Major elements

The Floreana clinopyroxenes analysed in this study (from scoria and xenolith samples) are augites ($En_{\sim 48.5}Fs_{\sim 8}Wo_{\sim 43.5}$) and have a relatively high Mg# (0.85–0.90; Mg# = Mg/(Mg+Fe_t) molar). The clinopyroxenes typically contain very high Na concentrations (<1.58 wt% Na_2O, <0.11 Na atoms per formula unit; Fig. 6A) and, correspondingly, up to 10% of the jadeite component. In general, clinopyroxene separates from scoria samples display a wide range of Na concentrations, whereas the xenolithic clinopyroxenes have high Na contents (Fig. 6A). The Floreana clinopyroxenes display a large range of Cr contents, ranging from <0.05 wt% in the most evolved crystals to ~1.72 wt% in the more primitive crystals (Fig. 6B).

5.3.2 Trace elements

Our Floreana clinopyroxenes display a wide range of geochemical enrichment, with LREE to MREE ratios varying from $[La/Sm]_n$ ~0.2 to $[La/Sm]_n$ ~3.1. Xenolithic clinopyroxenes typically have more enriched trace element ratios (such as $[La/Sm]_n$ or $[Ce/Y]_n$) than clinopyroxenes from the scoria samples (Fig. 7). Furthermore, the melt $[La/Sm]_n$ ratios calculated to be in equilibrium with clinopyroxenes from the scoria and xenolith samples range from ~1 to ~15 (calculated using the

elastic strain model of Wood and Blundy (1997) at 1225ºC and 700 MPa; Fig. 7B), significantly greater than the range measured in Floreana whole-rock samples (~2–5, with a small number of outliers up to ~7.5; Harpp et al. 2014a). Almost all of the xenolithic crystals, and a large proportion of the clinopyroxenes separated from scoria deposits, are too enriched to be in equilibrium with the typical composition of melts erupted on Floreana (Harpp et al.,2014a). In addition, there is a strong correlation between the Na concentrations and highly/moderately incompatible trace element ratios of the Floreana clinopyroxenes, such that crystal with high incompatible trace element concentrations typically contain a high jadeite component (Fig. 7A).

6 MAGMA SYSTEM ARCHITECTURE BENEATH ISLA FLOREANA

6.1 Mush crystallisation and textural equilibration

Based on pyroxene trace element and radiogenic isotope ratios, Lyons et al. (2007) hypothesised that gabbroic xenoliths in the Floreana lava and scoria deposits formed in an ancient (>1-1.5 Ma) magmatic system, compositionally similar to those currently beneath Cerro Azul and Sierra Negra volcanoes in the western Galápagos Archipelago. In contrast, wehrlite xenoliths preserve isotopic ratios similar to more recent subaerial lavas on Floreana, suggesting that they are fragments of the present-day magmatic system (Lyons et al., 2007).

Our wehrlitic xenoliths preserve an original igneous texture (clinopyroxene oikocrysts surrounding olivine chadacrysts; Wager et al., 1960) and display no evidence of textural re-equilibration (e.g. 120º dihedral angles) or metamorphic breakdown of plagioclase (e.g. pseudomorphs or relict cores; Lyons et al., 2007). The presence of orthopyroxene lamellae in some clinopyroxenes indicates that they cooled relatively slowly (Poldervaart and Hess, 1951). Hence, we suggest that the clinopyroxene crystals in our wehrlitic xenoliths grew within an olivine-dominated cumulate mush (i.e. interstitial growth of clinopyroxene oikocrysts; Wager et al., 1960). The rounded morphology and small size of olivine chadacrysts, relative to olivine crystals that are not enclosed by clinopyroxene oikocrysts (Fig. 3D), indicates that clinopyroxene growth may have been at the expense of olivine (e.g. Lissenberg

and MacLeod, 2016). If clinopyroxene growth is principally within a crystal-rich (i.e. relatively viscous and immobile) mush zone, this could explain its relatively low abundance in Floreana lava and scoria deposits (<5% of separated crystals).

In contrast with the wehrlites, three-grain plagioclase triple junctions in our gabbroic xenoliths have ~120° dihedral angles (Fig. 3A), indicating a high degree of textural equilibration (Holness et al., 2019, 2005). Plagioclase textural equilibrium, along with the two-pyroxene phase assemblage, suggests that the gabbroic xenoliths represent magmatic cumulates which were stored at high temperatures (>900°C) on long timescales (Holness et al., 2006). These petrographic observations are consistent with the gabbroic nodules sampling an ancient magmatic system beneath Floreana (>1 Ma; Lyons et al., 2007).

6.2 Mush disaggregation prior to eruption

6.2.1 Insights from olivine compositional heterogeneity

Olivine crystals separated from the Floreana lava and scoria samples have a wide range of zoning patterns, morphologies, and compositions (Fig. 2). The five olivine groups identified in the Floreana samples have distinct morphologies and zoning patterns (see Section 2 above), suggesting chemically heterogeneous magma storage (Holness et al., 2019). In particular, the most evolved crystals (Group 4; Fo~70–75) are in equilibrium with melts that are more evolved than the Floreana erupted basalts. This is consistent with a recent study which identified highly evolved (rhyolitic) magmas beneath basaltic volcanoes in the western Galápagos Archipelago (Stock et al., *in review*).

As Fe-Mg interdiffusion in olivine is geologically fast (Costa et al., 2020), preservation of forsterite zoning in the Floreana olivine crystals suggests that multiple magma batches interacted on relatively short pre-eruptive timescales. In Group 5 olivines, for example, four compositional zones are preserved over ~100-200 μm near the rim (Fig. 2E and F). Whilst we do not have enough Group 5 olivine crystals to calculate statistically robust timescales of pre-eruptive magma interactions using diffusion chronometry, complex forsterite zoning over ~100 μm is estimated to last <3 yrs at the approximate temperature of basaltic magma storage (~1225°C; using diffusion coefficients from Chakraborty, 2010). Therefore, we suggest that the range of crystal morphologies and major element

compositions displayed by the Floreana olivines in lava and scoria deposits indicates mixing and amalgamation of chemically heterogeneous magma storage regions over relatively short timescales prior to eruption.

The minor element chemistry of the olivine crystals allows us to investigate the crystallinity of these chemically diverse magma storage regions. Olivine crystals in our Floreana lava and scoria deposits have an unusually low, and large range of Ca concentrations (~250–2600 ppm compared with ~1500-3000 in the eastern Galápagos; Gleeson and Gibson, 2019; Fig. 5A). The lower end of the range in Ca concentrations measured in the Floreana lava and scoria deposits overlaps with those observed in cumulate xenoliths (wehrlites) and thus are unlikely to represent mantle olivines (Thompson and Gibson, 2000). Previous studies have shown that the Ca concentration of magmatic olivine is sensitive to several parameters, including: (i) the temperature of the system (Adams and Bishop, 1982; Köhler and Brey, 1990; Shejwalkar and Coogan, 2013); (ii) the H_2O content of the co-existing melt phase (Gavrilenko et al., 2016); and (iii) the major element composition of the co-existing melt phase (Herzberg, 2011). However, the diversity of Ca concentrations in our Floreana olivines is too large to be caused by variations in *T* alone (assuming that the difference between the crystallisation temperature and final storage temperature is <300°C; see Section 6.4). In addition, H_2O contents of ~3 wt% would be required to explain the lowest Ca concentrations in the Floreana olivines (according to the hygrometer of Gavrilenko et al., 2016), which is far in excess of that measure in Floreana submarine glasses by Peterson et al. (2017). Hence, Ca variations in Floreana olivines likely result from compositional variability in the co-existing melt phase.

Although olivine Ca variations are often interpreted to reflect lithological heterogeneity of the mantle source (resulting in primary melt compositional variability), this is inconsistent with the Ni contents of olivine crystals from Floreana (Fig. 5B; Gleeson and Gibson, 2019). An alternative process is therefore required to explain the variability of olivine Ca concentrations and, specifically, the presence of olivine crystals with <1000 ppm Ca. This process must reduce the Ca concentration of the melt phase (and co-existing olivines), without simultaneously reducing the melt Mg# (as low Ca

concentrations are observed across the entire range of forsterite contents in the Floreana olivines; Fig. 5A) and may be accompanied by slight variations in *T* or melt H_2O concentration.

Evidence for the origin of the low-Ca olivines in the lava and scoria deposits is present in texture and composition of the wehrlitic xenoliths, which contain uniformly low-Ca olivine crystals (<1000 ppm; Fig. 5A). The petrography of the wehrlitic xenoliths attests to clinopyroxene growth within olivine-dominated mush regions. Clinopyroxene crystallisation within this mush would extract CaO and MgO from the residual melt. However, in an olivine-rich mush, the large reservoir of MgO contained within the cumulus olivine grains would buffer the residual melt at a near-constant Mg# during clinopyroxene crystallisation (Meyer et al., 1989). In contrast, the CaO concentration of the melt is not buffered and decreasing melt CaO contents, due to clinopyroxene crystallisation, will cause the CaO concentration of cumulus olivine grains to decrease (as a result of diffusive re-equilibration). Intercumulus clinopyroxene growth would also increase the H_2O concentration of the residual melt phase, decreasing the partition coefficient of Ca into olivine (Gavrilenko et al., 2016). Therefore, if these mush-zone crystals are entrained into ascending melts prior to eruption, growth of clinopyroxene within an olivine-dominated mush could explain the presence of anomalously low Ca concentrations in the Floreana olivines separated from lava and scoria deposits.

As the majority of olivine analyses from the Floreana lava and scoria deposits have low Ca concentrations (<1000 ppm) that overlap with those in xenolithic nodules, we suggest that a large proportion of the erupted crystal cargo derives from highly crystalline magma storage regions. Higher Ca concentrations (>1500 ppm) are only found in a small number of forsteritic crystals (Fo>83) in the lava and scoria samples (Fig. 5A). As olivine crystals formed from peridotitic melts that have not undergone clinopyroxene growth will typically have Ca concentrations >1500 ppm (Gleeson and Gibson, 2019; Herzberg, 2011), we interpret these crystals to have grown within liquid-rich magma storage regions where magmatic differentiation occurs by fractional crystallisation.

However, olivine crystals from the Floreana lava and scoria deposits cannot simply be divided into low Ca (<1000 ppm) and high Ca (>1500 ppm) populations (Fig. 5A). A substantial number of olivine crystals have intermediate compositions (Ca = 1000–1500). We interpret these as being sourced from

392 regions where growth of clinopyroxene was ongoing at the time of mush disaggregation. Thus, the
393 olivine crystal cargo of the Floreana magmas is predominantly derived from crystal-rich domains that
394 vary from highly crystalline (Ca <1000 ppm) to moderately crystalline (Ca = 1000–1500 ppm). Only
395 a small number of olivine crystals preserve compositions consistent with fractional crystallisation in
396 liquid-rich storage regions (Ca >1500 ppm).

397 *6.2.2 Insights from clinopyroxene major element compositions*
398 The compositions of clinopyroxene crystals from the Floreana scoria also overlap with those in our
399 xenolith samples, supporting the hypothesis that some of the erupted crystals are derived from
400 disaggregated sub-volcanic mush. We used hierarchical cluster analysis to subdivide our 567
401 clinopyroxene major element analyses from the Floreana scoria and xenolith samples to determine the
402 proportion of material that is derived from each xenolith lithology in the erupted crystal cargo. We
403 find that our clinopyroxene analyses form three distinct groups (Fig. 8):

404 - Group 1 clinopyroxenes are predominantly from the wehlite and dunite xenoliths and include
405 90% of our analyses from these samples. 39% of clinopyroxenes analysed from the scoria
406 samples also fall into this group.
407 - Group 2 clinopyroxenes include all analyses from the gabbroic xenoliths, and ~10% of
408 analyses from crystals separated from the scoria samples.
409 - Group 3 clinopyroxenes are dominantly analyses from scoria derived clinopyroxenes (~50%
410 of analyses from the scoria separates). However, 10% of analyses from the wehrlite and
411 dunite xenoliths also fall into this group.

412 Of our 248 clinopyroxenes analysed from the Floreana scoria samples, approximately half are
413 classified as Group 3 and thus have major element compositions that do not show any affinity to
414 either the wehrlite/dunite or gabbroic cumulates. Therefore, these crystals may represent autocrysts
415 (with growth in liquid-rich magma storage regions). The remainder of clinopyroxene analyses from
416 the scoria samples are either compositionally analogous to those in the wehrlite and dunite xenoliths
417 (Group 1; 39%) or the gabbroic xenoliths (Group 2; 11%); we interpret these as representing
418 disaggregated sub-volcanic mush or wall rock. The high proportion of the clinopyroxene crystal cargo

that is derived from highly crystalline storage regions beneath Floreana is consistent with our interpretation of olivine minor element concentrations.

6.3 Reactive Porous Flow within a cumulate mush

Whilst the olivine and clinopyroxene major and minor element concentrations show that a large proportion of the erupted crystal cargo is derived from highly crystalline magma storage regions, clinopyroxene trace element concentrations (and zoning) reveal the magmatic processes that operate within these crystal-rich domains. The trace element composition of melts in equilibrium with our clinopyroxene crystals are calculated using the model of Wood and Blundy (1997). The results indicate that many of our clinopyroxene analyses have incompatible trace element ratios (e.g. $[Ce/Y]_n$) which are more enriched than any erupted basalt from Floreana (Harpp et al., 2014a). In fact, nearly all clinopyroxenes analyses from our xenolith samples, and ~50% of clinopyroxene analyses from the scoria samples, record trace element disequilibrium with the typical trace element composition of the Floreana basalts (Fig. 7 and 9). Over-enriched equilibrium melt signatures are characteristics of Group 1 clinopyroxenes (i.e. chemical affinity to the wehrlitic or dunitic xenoliths), whereas crystals that are near trace element equilibrium with Floreana basalts typically have Group 3 major element compositions (i.e. the autocryst group).

Petrographic observations and olivine minor element data indicate that the Floreana sub-volcanic system is characterised by clinopyroxene crystallisation within an olivine-dominated mush. If the clinopyroxene grew from trapped melt within an olivine-dominated mush, progressive crystallisation would increase the concentration of highly incompatible trace elements (e.g. Ba, La, Ce) relative to less incompatible trace-elements (e.g. Sm, Y) in the residual melt. A simple fractional crystallisation model indicates that ~80% crystallisation is required to generate melt $[Ce/Y]_n$ ratios that are in equilibrium with enriched clinopyroxenes from the scoria samples and even greater extents of crystallisation (~90%) would be required to generate the extremely high $[Ce/Y]_n$ ratios in some of the xenolithic clinopyroxenes (Fig. 9). Such extensive crystallisation would be expected to result in the saturation and crystallisation of plagioclase and other accessory phases (e.g. apatite,

magnetite/ilmenite, quartz), which are observed in more evolved xenoliths from Rabida island in the central Galápagos (Holness et al., 2019). However, these phases are absent in the Floreana xenoliths, indicating that another process is responsible for generating the anomalous trace element signatures of the melts in equilibrium with our clinopyroxenes.

One possible mechanism for generating the observed trace element over-enrichment is reactive porous flow, where clinopyroxene saturated melts ascend through highly-crystalline magmatic systems causing dissolution of the existing crystal framework and precipitation of clinopyroxene (Lissenberg and MacLeod, 2016). Reactive porous flow can result in net replacement of olivine by clinopyroxene, leading to enrichment of highly- to moderately-incompatible trace elements in the resulting melt and co-existing crystal phases (Coogan et al., 2000; Gao et al., 2007; Lissenberg et al., 2013; Lissenberg and MacLeod, 2016), and is consistent with the petrography of the Floreana xenoliths. For example, major element maps of clinopyroxene crystals in the Floreana wehrlites show that they are zoned, with Ti-rich rims (Fig. 10); equivalent zoning patterns have been attributed to reactive porous flow in plutonic clinopyroxenes from the oceanic crust (e.g. Hess Deep; Lissenberg and MacLeod, 2016). Furthermore, reactive porous flow is consistent with the small size and rounded morphology of olivine chadacrysts. In addition, if pre-existing Cr-spinel was dissolved by the reacting melt, then reactive porous flow could also explain the high Cr contents of clinopyroxene in our wehrlitic xenoliths (Fig. 6; Lissenberg and MacLeod, 2016).

To test whether reactive porous flow of clinopyroxene saturated melts through an olivine-dominated mush is consistent with the trace element compositions of melts calculated to be in equilibrium with our Floreana clinopyroxenes, we use the zone refining model of Harris (1957; Fig. 9):

$$\frac{C_l}{C_l^o} = \frac{1}{D} - (\frac{1}{D} - 1)^{-DI} \quad \text{(eq. 1)}$$

where D is the bulk partition coefficient; C_l^o and C_l are the initial and final concentration of that element in the melt phase, respectively; and I is the 'equivalent volumes of solid processed by the

liquid' (Lissenberg and MacLeod, 2016). The model assumes that a migrating melt front depletes solid phases of their incompatible trace elements owing to partial melting, and has previously been employed to investigate geochemical signatures in oceanic gabbros (Lissenberg and MacLeod, 2016). The model produces melts with trace element compositions that are comparable with those in equilibrium with our Floreana clinopyroxenes (i.e. $[Ce/Y]_n$ ~8-13) using I values similar to that invoked in other magmatic settings worldwide (~4–10; Lissenberg and MacLeod, 2016). Hence, reactive porous flow represents a realistic mechanism for generating the geochemical diversity of Floreana clinopyroxenes, including the trace element enriched crystals analysed in the wehrlitic nodules (Fig. 9).

In addition, detailed LA-ICP-MS transects of two clinopyroxene grains from the most enriched wehrlitic xenolith analysed in this study (17MMSG02c) show clear trace element zoning (Fig. 11). The core of the larger clinopyroxene crystal has low [Ce] and $[Ce/Y]_n$ contents that are approximately in equilibrium with Floreana basalts (Harpp et al. 2014a; Fig. 11a), whereas the mantle is characterised by increasing [Ce] and $[Ce/Y]_n$ contents towards the rim. We interpret this as core crystallisation from a melt with a trace element signature similar to that of erupted Floreana basalts (Harpp et al., 2014a), followed by growth from a melt which became progressively enriched during reactive porous flow (Fig. 11).

The mantle of the second, smaller xenolithic clinopyroxene shows a similar rim-ward increase in [Ce] (interpreted as progressive melt enrichment during reactive porous flow). However, the [Ce] and $[Ce/Y]_n$ values of the crystal core are too high to be in equilibrium with erupted Floreana basalts (Fig. 11C). This is consistent with spot analyses of clinopyroxene cores in other crystals analysed in this study. The high [Ce] and $[Ce/Y]_n$ values in crystal cores cannot be explained by inward diffusion of Ce, owing to significant differences in the diffusivities of Ce and Y and similar [Ce] and [Y] zoning patterns in our two crystal transects (Fig. 11; Van Orman, 2001). Instead, we suggest that the high apparent core [Ce] and $[Ce/Y]_n$ contents in many of the Floreana clinopyroxenes record crystallisation from melts that had already undergone geochemical enrichment via reactive porous flow. However, we cannot discount that our apparent clinopyroxene cores are fragments of larger oikocrysts that have

been broken during mush disaggregation or sample crushing and, as a result, do not represent the true core compositions of each crystal.

Nevertheless, our clinopyroxene major and trace element data, as well as petrographic observations of the wehrlitic xenoliths, provide substantial evidence that reactive porous flow is an important mechanism of melt migration and melt differentiation in highly crystalline magma storage regions beneath Floreana. Although reactive porous flow has been identified as an important process in MOR gabbros, this is the first study to identify reactive porous flow in an ocean island setting.

6.4 Petrographic estimates of magma storage pressures

Petrological and geophysical constraints on magma storage depths exist for several recently active volcanoes in the western Galápagos Archipelago (Bagnardi et al., 2013; Case et al., 1973; Geist et al., 1998; Stock et al., 2018; Vigouroux et al., 2008). However, in the absence of geophysical data (owing to a paucity of recent eruptions), there are far fewer constraints on the structure of magma storage regions in the eastern and south-eastern archipelago. To date, the only investigation of magma storage depths beneath these volcanoes is by Geist et al. (1998), who undertook a visual comparison between whole-rock lava compositions and the MORB olivine + plagioclase + augite + melt pseudoinvariant point, parameterised by Grove et al. (1992). This approach is subject to substantial uncertainty, but the authors suggest that Floreana magmas consistently equilibrate at >5 kbar (typically >7 kbar) at a depth >16 km, within the upper mantle.

We used three petrological barometers to provide improved constraints on magma storage depths beneath Floreana. First, we applied the clinopyroxene-only barometer of Putirka (2008), in which pressure and temperature are solved iteratively based solely on the clinopyroxene major element composition (primarily the jadeite component; standard error of estimate [SEE] = ±310 MPa). Second, we applied the clinopyroxene-melt barometer of Neave and Putirka (2017), which uses the composition of a co-existing melt phase and the proportion of the Jadeite component in clinopyroxene to calculate the pressure of crystallisation (SEE = ±140 MPa; pressure is solved iteratively with temperature using the clinopyroxene-melt thermometer of Putirka, 2008). Third, for the xenolithic

nodules, we estimate the final pressure and temperature of storage using the two-pyroxene thermobarometer of Putirka (2008) (SEE = ±260 MPa).

Taken at face value, initial application of the clinopyroxene-only barometer to all clinopyroxene analyses from the scoria and xenolith samples gives a range of pressure estimates between ~450 MPa and ~1800 MPa. However, reactive porous flow has a substantial influence on the compositions of the Group 1 (and Group 2) clinopyroxenes, which may influence the barometric results. Specifically, crystals that show evidence for reactive porous flow also have elevated Na concentrations, leading to an anomalously high jadite component. Therefore, we filter our dataset to remove crystals that show a chemical signature indicative of reactive porous flow and only use Group 3 clinopyroxenes that have trace element compositions in equilibrium with the Floreana basalts (using the whole-rock data from Harpp et al. 2014) in our barometric calculations (n=78). Results indicate that crystallisation beneath Floreana occurs at a pressure of 766 ±322 MPa (2σ of calculated pressures), which equates to a depth of 25.2 ±9.9 km (using the crustal density estimate of Putirka (1997) and a mantle density estimate of 3300 km/m^3; Fig. 12).

Application of the Neave and Putirka (2017) clinopyroxene-melt barometer requires identification of equilibrium clinopyroxene-liquid pairs. We achieve this using an automated melt-matching algorithm (as in Winpenny and Maclennan, 2011, Neave and Putirka, 2017, Stock et al. 2018), with K_D(Fe-Mg), diopside-hedenbergite, enstatite-ferrosillite and calcium Tschermak's equilibrium tests (K_D(Fe-Mg) within ±0.03 other components within 2 SEE; Putirka, 1999, Putirka, 2008, Mollo et al., 2013). We used the whole-rock data of Harpp et al. (2014a) and basaltic glass analyses from this study as potential equilibrium liquids. Input crystal compositions were again filtered to remove analyses that showed evidence of reactive porous flow (i.e. only Group 3 clinopyroxenes in equilibrium with the Floreana whole-rock were used). In total, 70 of the 78 input clinopyroxene analyses returned at least one equilibrium match to either the basaltic glass or whole-rock compositions. Where clinopyroxene compositions produced an equilibrium match with more than one equilibrium melt, an average melt composition was used in the barometric model. Results from this barometer indicate that magma crystallisation occurred at 717 ±165 MPa (23.7 ±5.1 km) and 1224 ±33°C (Fig. 12).

Clinopyroxene-orthopyroxene thermobarometry records the final storage conditions of the cumulate xenoliths, rather than the crystallisation conditions of clinopyroxene autocrysts (orthopyroxene is only found as an intercumulus phase). Temperature and pressure estimates were only calculated from orthopyroxene-clinopyroxene pairs in wehrlite and dunite xenoliths that passed the K_D(Fe-Mg) equilibrium test of Putirka (2008; within ±0.14). Results suggest that the cumulates were stored at ~975–1100ºC and 600–900 MPa, with a mean storage pressure of 712 ±200 MPa (23.7 ±6.4 km; Fig. 12).

The depths of magma storage calculated from our three petrological barometers show an excellent agreement within the model uncertainties. These new data provide robust evidence that magma storage beneath Floreana occurs below the Moho (~16 km; Feighner and Richards, 1994), in the upper mantle.

7 IMPLICATIONS FOR MAGMATIC PLUMBING SYSTEMS BENEATH LOW MELT FLUX OCEAN ISLAND VOLCANOES

Our new petrological and geochemical data show that magma storage beneath Floreana occurs in mush-dominated regions in the upper mantle (Fig. 13). Mineral chemistry (such as low olivine Ca concentrations and clinopyroxene major elements) reveal that a substantial portion of the erupted crystal cargo is derived from disaggregated mush and wall rock material which has been entrained into the ascending magmas. During ascent, magmas may entrain coherent nodules (xenoliths) as well as disaggregated mush (Fig. 13). Coherent nodules represent areas of the magmatic system beneath Floreana that have undergone cooling to temperatures <1100ºC (compared to the clinopyroxene crystallisation temperatures of ~1225ºC) and may represent material from the border of the active mush zone or older, almost completely solidified magma storage regions that are intersected during magma ascent (Fig. 13).

Petrographic observations and clinopyroxene trace element chemistry from both the xenolith and scoria samples reveal that clinopyroxene growth occurs via reactive porous flow in the mush-

dominated areas beneath Floreana. Reactive porous flow causes distinct trace element enrichment in the percolating melt phase and crystallising clinopyroxene, which can explain the trace element disequilibrium between the erupted Floreana basalts and their clinopyroxene cargo. Nevertheless, the presence of some clinopyroxene crystals with major and trace element compositions in equilibrium with erupted Floreana basalts indicates that at least some crystallisation occurs in liquid-rich sub-volcanic storage regions, likely situated as localised melt pockets within the larger mush zone (Fig. 13). Transport of melts modified by reactive porous flow into these melt pockets could impact the LREE enriched signature of the resultant hybridised melts. This could explain the LREE-enriched signature in the Floreana basalts, which is not seen in other regions of the Galápagos Archipelago (Harpp et al., 2014a).

Our results indicate substantial differences in the architecture of the magmatic systems beneath Floreana and the frequently active shield volcanoes in the western Galápagos Archipelago. For example, previous petrological and geophysical studies have identified that western Galápagos magmatic systems are characterised by crustal magma storage, often with a large storage region in the mid-to-lower crust (~7 km depth) and a smaller storage region at shallow levels, within the volcanic edifice (~1 km depth; Geist et al. 1998; Bagnardi et al. 2013; Bagnardi and Hooper, 2018; Stock et al., 2018; Fig 12). In contrast, our barometric data indicate that magmas beneath Floreana ascend directly from the upper mantle and undergo no detectable crustal storage. Although mush-rich regions have been inferred beneath the western Galápagos shield volcanoes (based on whole-rock data and the presence of gabbroic glomerocrysts; Chadwick et al., 2011; Geist et al., 1995, 2014; Stock et al., 2018), magmatic differentiation appears to be driven by simple fractional crystallisation and mixing of chemically diverse magmas (Geist et al., 1995; Naumann and Geist, 1999; Stock et al., *in review*).

One major factor that differentiates Floreana from shield volcanoes in the western archipelago (on Isabela and Fernandina) is the flux of magma into the lithosphere, as evidenced by variations in the volumetric eruption rate (Harpp et al., 2014a; Harpp and Geist, 2018; Kurz et al., 2014). Hence, we suggest that the greater pressure of magma storage and prevalence of reactive porous flow beneath Floreana, relative to volcanoes in the western archipelago, are related to the substantially lower flux of

603 magma into the lithosphere from the underlying mantle source (and thus the thermal structure of the
604 lithosphere). For example, the magma flux entering the lithosphere beneath Wolf volcano (northern
605 Isabela) has been substantially greater than that beneath Floreana for several 100,000s of years. The
606 high magma flux beneath Wolf maintains the average temperature of the mid-to-lower crust at
607 ~1125ºC (ΔT ~22 ºC), with only small-scale thermal and compositional heterogeneities present in the
608 sub-volcanic plumbing system (Geist et al., 2014, 2005; Stock et al., 2018, *in review*). In contrast, the
609 flux of magma entering the magmatic system beneath Floreana is much lower and the temperature of
610 the mid-crust is likely to be <<800ºC (i.e. significantly cooler than the lowest temperature recorded by
611 the Floreana xenoliths; Fig. 12). As the flux of magma (and heat) from the mantle is insufficient to
612 maintain an elevated crustal geotherm beneath Floreana, magmas that stall in the crust are likely to
613 rapidly crystallise, increase their viscosity, and become uneruptable. Therefore, eruptions must be fed
614 by melts ascending from much deeper storage regions (~700-750 MPa) where super-solidus melts can
615 persist over long time periods.

616 Our results have global implications for the architecture and dynamics of magma storage regions
617 beneath ocean island volcanoes that are characterised by a relatively low flux of magma from the
618 underlying mantle. These include off-axis volcanic systems (e.g. Halekala, Hawaii) and those above
619 low buoyancy flux mantle plumes (e.g. El Hierro, Canary Islands). Figure 14 shows a compilation of
620 published barometric estimates from 'high' and 'low' melt flux systems in some of the most active
621 ocean island systems on Earth (Hawaii, Iceland and Galápagos; Hammer et al., 2016; Hartley et al.,
622 2018; Neave and Putirka, 2017; Poland et al., 2015; Stock et al., 2018). Central volcanic systems from
623 each region typically display relatively low-pressure magma storage compared to regions that are
624 characterised by a comparatively low magma flux from the convecting mantle (i.e. off-axis volcanic
625 systems; Fig. 14). This observation is consistent with the high pressures of magma storage identified
626 at other ocean island volcanoes that are located above mantle plumes with a relatively low buoyancy
627 flux (e.g. >15-25 km at El Hierro in the Canary Islands; Longpre et al., 2014; Taracsák et al., 2019).
628 Hence, we speculate that high-pressure magma storage is characteristic of low melt flux ocean island
629 volcanoes globally.

8 CONCLUSIONS

Petrographic and geochemical analyses of lava, scoria and xenolith samples from Floreana in the south-eastern Galápagos Archipelago provide new insights into the architecture and dynamics of magma storage beneath low melt flux ocean island volcanoes. Comparison of olivine and clinopyroxene major, minor and trace element contents between our different sample types reveals that a substantial portion of the erupted crystal cargo is derived from mush-dominated magma storage regions beneath Floreana. Mineral textures, highly enriched clinopyroxene trace element signatures and trace element zoning in the xenoliths reveals that reactive porous flow is an important process of chemical differentiation and melt transport within these mush-dominated regions. Mixing between melts that have been geochemically enriched by reactive porous flow and those in overlying liquid-rich storage regions could explain the anomalous LREE enriched signature of the Floreana basalts, which is absent in other parts of the Galápagos Archipelago where reactive porous flow has not been identified.

Application of independent petrological barometers to crystals in Floreana scoria and xenolith samples indicates that magmas are stored in the upper mantle (~23.7 ±5.1 km). Floreana is in a distal location to the Galápagos plume where the melt flux entering the lithosphere is low; the depth of magma storage beneath Floreana contrasts with more proximal, higher melt flux volcanoes in the western archipelago where magmas are stored in the crust (Geist et al., 1998; Stock et al., 2018). Comparing our new data with ocean island volcanoes globally (e.g. Hawaii, Iceland and the Canary Islands) reveals that the Galápagos is not unique and that magma storage is ubiquitously shallower in proximal magmatic systems above high buoyancy flux plumes than in off-axis systems, or above low buoyancy flux plumes. We therefore suggest that the flux of mantle-derived magma entering the lithosphere imparts a first-order control on the depth of magma storage beneath ocean island volcanoes.

ACKNOWLEDGEMENTS

This study was supported by a NERC (Natural Environmental Research Council) Research Training Student Grant (NE/L002507/1) awarded to M.L.M.G as well as NERC grant awared to S.A.G

RG57434. M. J. S. was supported by a Charles Darwin and Galápagos Islands Junior Research Fellowship at Christ's College, Cambridge. We are grateful to Iris Buisman and Jason Day for their help with electron microprobe and laser-ablation inductively-coupled mass spectrometry analysis, respectively. We also thank Dr Margaret Hartley for her comments on an early version of this manuscript.

REFERENCES

Adams, G.E., Bishop, F.C., 1982. Experimental investigation of CaMg exchange between olivine, orthopyroxene, and clinopyroxene: potential for geobarometry. Earth Planet. Sci. Lett. 57, 241–250. https://doi.org/10.1016/0012-821X(82)90188-1

Allan, J.F., Simkin, T., 2000. Fernandina Volcano's evolved, well-mixed basalts: Mineralogical and petrological constraints on the nature of the Galápagos plume. J. Geophys. Res. Solid Earth 105, 6017–6041. https://doi.org/10.1029/1999JB900417

Amelung, F., Jónsson, S., Zebker, H., Segall, P., 2000. Widespread uplift and 'trapdoor' faulting on Galápagos volcanoes observed with radar interferometry. Nature 407, 993–996. https://doi.org/10.1038/35039604

Asimow, P.D., Langmuir, C.H., 2003. The importance of water to oceanic mantle melting regimes. Nature 421, 815–820. https://doi.org/10.1038/nature01429

Bagnardi, M., Amelung, F., Poland, M.P., 2013. A new model for the growth of basaltic shields based on deformation of Fernandina volcano, Galápagos Islands. Earth Planet. Sci. Lett. 377–378, 358–366. https://doi.org/10.1016/j.epsl.2013.07.016

Bailey, K., 1976. Potassium-Argon Ages from the Galápagos Islands. Science 192, 465–467. https://doi.org/10.1126/science.192.4238.465

Barker, S.J., Rowe, M.C., Wilson, C.J.N., Gamble, J.A., Rooyakkers, S.M., Wysoczanski, R.J., Illsley-Kemp, F., Kenworthy, C.C., 2020. What lies beneath? Reconstructing the primitive magmas fueling voluminous silicic volcanism using olivine-hosted melt inclusions.

Case, J.E., Ryland, S.L., Simkin, T., Howard, K.A., 1973. Gravitational Evidence for a Low-Density Mass beneath the Galápagos Islands. Science 181, 1040–1042. https://doi.org/10.1126/science.181.4104.1040

Chadwick, W.W., Howard, K.A., 1991. The pattern of circumferential and radial eruptive fissures on the volcanoes of Fernandina and Isabela islands, Galápagos. Bull. Volcanol. 53, 259–275. https://doi.org/10.1007/BF00414523

Chadwick, W.W., Jónsson, S., Geist, D.J., Poland, M., Johnson, D.J., Batt, S., Harpp, K.S., Ruiz, A., 2011. The May 2005 eruption of Fernandina volcano, Galápagos: The first circumferential dike intrusion observed by GPS and InSAR. Bull. Volcanol. 73, 679–697. https://doi.org/10.1007/s00445-010-0433-0

Chakraborty, S., 2010. Diffusion Coefficients in Olivine, Wadsleyite and Ringwoodite. Rev. Mineral. Geochem. 72, 603–639. https://doi.org/10.2138/rmg.2010.72.13

Clague, D.A., Denlinger, R.P., 1994. Role of olivine cumulates in destabilizing the flanks of Hawaiian volcanoes. Bull. Volcanol. 56, 425–434. https://doi.org/10.1007/BF00302824

Cleary, Z., Schwartz, D.M., Mittelstaedt, E., Harpp, K., 2020. Dynamic Magma Storage at Near-Ridge Hot Spots: Evidence From New Galápagos Gravity Data. Geochem. Geophys. Geosystems 21. https://doi.org/10.1029/2019GC008722

Coogan, L.A., Saunders, A.D., Kempton, P.D., Norry, M.J., 2000. Evidence from oceanic gabbros for porous melt migration within a crystal mush beneath the Mid-Atlantic Ridge. Geochem. Geophys. Geosystems 1, n/a-n/a. https://doi.org/10.1029/2000GC000072

Costa, F., Shea, T., Ubide, T., 2020. Diffusion chronometry and the timescales of magmatic processes. Nat. Rev. Earth Environ. https://doi.org/10.1038/s43017-020-0038-x

Davidge, L., Ebinger, C., Ruiz, M., Tepp, G., Amelung, F., Geist, D., Coté, D., Anzieta, J., 2017. Seismicity patterns during a period of inflation at Sierra Negra volcano, Galápagos Ocean Island Chain. Earth Planet. Sci. Lett. 462, 169–179. https://doi.org/10.1016/j.epsl.2016.12.021

Donaldson, C.H., 1976. An experimental investigation of olivine morphology. Contrib. Mineral. Petrol. 57, 187–213. https://doi.org/10.1007/BF00405225

Feighner, M.A., Richards, M.A., 1994. Lithospheric structure and compensation mechanisms of the Galápagos Archipelago. J. Geophys. Res. 99, 6711. https://doi.org/10.1029/93JB03360

Gao, Y., Hoefs, J., Hellebrand, E., von der Handt, A., Snow, J.E., 2007. Trace element zoning in pyroxenes from ODP Hole 735B gabbros: diffusive exchange or synkinematic crystal fractionation? Contrib. Mineral. Petrol. 153, 429–442. https://doi.org/10.1007/s00410-006-0158-4

Gavrilenko, M., Herzberg, C., Vidito, C., Carr, M.J., Tenner, T., Ozerov, A., 2016. A Calcium-in-Olivine Geohygrometer and its Application to Subduction Zone Magmatism. J. Petrol. 57, 1811–1832. https://doi.org/10.1093/petrology/egw062

Geist, D., Howard, K.A., Larson, P., 1995. The Generation of Oceanic Rhyolites by Crystal Fractionation: the Basalt-Rhyolite Association at Volc n Alcedo, Galápagos Archipelago. J. Petrol. 36, 965–982. https://doi.org/10.1093/petrology/36.4.965

Geist, D., Naumann, T., Larson, P., 1998. Evolution of Galápagos Magmas: Mantle and Crustal Fractionation without Assimilation. J. Petrol. 39, 953–971. https://doi.org/10.1093/petroj/39.5.953

Geist, D., White, W.M., Albarede, F., Harpp, K., Reynolds, R., Blichert-Toft, J., Kurz, M.D., 2002. Volcanic evolution in the Galápagos: The dissected shield of Volcan Ecuador. Geochem. Geophys. Geosystems 3, 1 of 32–32 32. https://doi.org/10.1029/2002GC000355

Geist, D.J., Bergantz, G., Chadwick, W.W., 2014. Galápagos Magma Chambers, in: Harpp, K.S., Mittelstaedt, E., d'Ozouville, N., Graham, D.W. (Eds.), Geophysical Monograph Series. John Wiley & Sons, Inc, Hoboken, New Jersey, pp. 55–69. https://doi.org/10.1002/9781118852538.ch5

Geist, D.J., Fornari, D.J., Kurz, M.D., Harpp, K.S., Adam Soule, S., Perfit, M.R., Koleszar, A.M., 2006. Submarine Fernandina: Magmatism at the leading edge of the Galápagos hot spot. Geochem. Geophys. Geosystems 7, n/a-n/a. https://doi.org/10.1029/2006GC001290

Geist, D.J., McBIRNEY, A.R., Duncan, R.A., 1986. Geology and petrogenesis of lavas from San Cristobal Island, Galápagos Archipelago. Geol. Soc. Am. Bull. 97, 555. https://doi.org/10.1130/0016-7606(1986)97<555:GAPOLF>2.0.CO;2

Geist, D.J., Naumann, T.R., Standish, J.J., Kurz, M.D., Harpp, K.S., White, W.M., Fornari, D.J., 2005. Wolf Volcano, Galápagos Archipelago: Melting and Magmatic Evolution at the Margins of a Mantle Plume. J. Petrol. 46, 2197–2224. https://doi.org/10.1093/petrology/egi052

Geist, D.J., White, W.M., McBirney, A.R., 1988. Plume-asthenosphere mixing beneath the Galápagos archipelago. Nature 333, 657–660. https://doi.org/10.1038/333657a0

Gibson, S.A., Dale, C.W., Geist, D.J., Day, J.A., Brügmann, G., Harpp, K.S., 2016. The influence of melt flux and crustal processing on Re–Os isotope systematics of ocean island basalts: Constraints from Galápagos. Earth Planet. Sci. Lett. 449, 345–359. https://doi.org/10.1016/j.epsl.2016.05.021

Gibson, S.A., Geist, D., 2010. Geochemical and geophysical estimates of lithospheric thickness variation beneath Galápagos. Earth Planet. Sci. Lett. 300, 275–286. https://doi.org/10.1016/j.epsl.2010.10.002

Gibson, S.A., Geist, D.G., Day, J.A., Dale, C.W., 2012. Short wavelength heterogeneity in the Galápagos plume: Evidence from compositionally diverse basalts on Isla Santiago. Geochem. Geophys. Geosystems 13. https://doi.org/10.1029/2012GC004244

Gleeson, M.L.M., Gibson, S.A., 2019. Crustal controls on apparent mantle pyroxenite signals in ocean-island basalts. Geology. https://doi.org/10.1130/G45759.1

Gleeson, M.L.M., Gibson, S.A., Williams, H.M., 2020. Novel insights from Fe-isotopes into the lithological heterogeneity of Ocean Island Basalts and plume-influenced MORBs. Earth Planet. Sci. Lett. 535, 116114. https://doi.org/10.1016/j.epsl.2020.116114

Grove, T.L., Kinzler, R.J., Bryan, W.B., 1992. Fractionation of Mid-Ocean Ridge Basalt (MORB), in: Morgan, J.P., Blackman, D.K., Sinton, J.M. (Eds.), Geophysical Monograph Series. American Geophysical Union, Washington, D. C., pp. 281–310. https://doi.org/10.1029/GM071p0281

761 Hammer, J., Jacob, S., Welsch, B., Hellebrand, E., Sinton, J., 2016. Clinopyroxene in postshield
762 Haleakala ankaramite: 1. Efficacy of thermobarometry. Contrib. Mineral. Petrol. 171, 7.
763 https://doi.org/10.1007/s00410-015-1212-x
764 Harpp, K.S., Geist, D.J., 2018. The Evolution of Galápagos Volcanoes: An Alternative Perspective.
765 Front. Earth Sci. 6. https://doi.org/10.3389/feart.2018.00050
766 Harpp, K.S., Geist, D.J., Koleszar, A.M., Christensen, B., Lyons, J., Sabga, M., Rollins, N., 2014a.
767 The Geology and Geochemistry of Isla Floreana, Galápagos: A Different Type of Late-Stage
768 Ocean Island Volcanism, in: Harpp, K.S., Mittelstaedt, E., d'Ozouville, N., Graham, D.W.
769 (Eds.), Geophysical Monograph Series. John Wiley & Sons, Inc, Hoboken, New Jersey, pp.
770 71–117. https://doi.org/10.1002/9781118852538.ch6
771 Harpp, K.S., White, W.M., 2001. Tracing a mantle plume: Isotopic and trace element variations of
772 Galápagos seamounts. Geochem. Geophys. Geosystems 2, n/a-n/a.
773 https://doi.org/10.1029/2000GC000137
774 Harpp, K.S., Wirth, K.R., Teasdale, R., Blair, S., Reed, L., Barr, J., Pistiner, J., Korich, D., 2014b.
775 Plume-Ridge Interaction in the Galápagos: Perspectives from Wolf, Darwin, and Genovesa
776 Islands, in: Harpp, K.S., Mittelstaedt, E., d'Ozouville, N., Graham, D.W. (Eds.), Geophysical
777 Monograph Series. John Wiley & Sons, Inc, Hoboken, New Jersey, pp. 285–334.
778 https://doi.org/10.1002/9781118852538.ch15
779 Harris, P.G., 1957. Zone refining and the origin of potassic basalts. Geochim. Cosmochim. Acta 12,
780 195–208. https://doi.org/10.1016/0016-7037(57)90032-7
781 Hartley, M.E., Bali, E., Maclennan, J., Neave, D.A., Halldórsson, S.A., 2018. Melt inclusion
782 constraints on petrogenesis of the 2014–2015 Holuhraun eruption, Iceland. Contrib. Mineral.
783 Petrol. 173. https://doi.org/10.1007/s00410-017-1435-0
784 Herzberg, C., 2011. Identification of Source Lithology in the Hawaiian and Canary Islands:
785 Implications for Origins. J. Petrol. 52, 113–146. https://doi.org/10.1093/petrology/egq075
786 Holness, M.B., Cheadle, M.J., McKenkie, D., 2005. On the Use of Changes in Dihedral Angle to
787 Decode Late-stage Textural Evolution in Cumulates. J. Petrol. 46, 1565–1583.
788 https://doi.org/10.1093/petrology/egi026
789 Holness, M.B., Nielsen, T.F.D., Tegner, C., 2006. Textural Maturity of Cumulates: a Record of
790 Chamber Filling, Liquidus Assemblage, Cooling Rate and Large-scale Convection in Mafic
791 Layered Intrusions. J. Petrol. 48, 141–157. https://doi.org/10.1093/petrology/egl057
792 Holness, M.B., Stock, M.J., Geist, D., 2019. Magma chambers versus mush zones: constraining the
793 architecture of sub-volcanic plumbing systems from microstructural analysis of crystalline
794 enclaves. Philos. Trans. R. Soc. Math. Phys. Eng. Sci. 377, 20180006.
795 https://doi.org/10.1098/rsta.2018.0006
796 Jackson, M.G., Konter, J.G., Becker, T.W., 2017. Primordial helium entrained by the hottest mantle
797 plumes. Nature 542, 340–343. https://doi.org/10.1038/nature21023
798 Jarosewich, E., Nelen, J.A., Norberg, J.A., 1980. Reference Samples for Electron Microprobe
799 Analysis*. Geostand. Geoanalytical Res. 4, 43–47. https://doi.org/10.1111/j.1751-
800 908X.1980.tb00273.x
801 Jochum, K.P., Weis, U., Schwager, B., Stoll, B., Wilson, S.A., Haug, G.H., Andreae, M.O.,
802 Enzweiler, J., 2016. Reference Values Following ISO Guidelines for Frequently Requested
803 Rock Reference Materials. Geostand. Geoanalytical Res. 40, 333–350.
804 https://doi.org/10.1111/j.1751-908X.2015.00392.x
805 Kilbride, B.M., Edmonds, M., Biggs, J., 2016. Observing eruptions of gas-rich compressible magmas
806 from space. Nat. Commun. 7, 13744. https://doi.org/10.1038/ncomms13744
807 Köhler, T.P., Brey, G.P., 1990. Calcium exchange between olivine and clinopyroxene calibrated as a
808 geothermobarometer for natural peridotites from 2 to 60 kb with applications. Geochim.
809 Cosmochim. Acta 54, 2375–2388. https://doi.org/10.1016/0016-7037(90)90226-B
810 Kurz, M.D., Rowland, S.K., Curtice, J., Saal, A.E., Naumann, T., 2014. Eruption Rates for Fernandina
811 Volcano: A New Chronology at the Galápagos Hotspot Center, in: Harpp, K.S., Mittelstaedt,
812 E., d'Ozouville, N., Graham, D.W. (Eds.), Geophysical Monograph Series. John Wiley &
813 Sons, Inc, Hoboken, New Jersey, pp. 41–54. https://doi.org/10.1002/9781118852538.ch4
814 Lissenberg, C.J., MacLeod, C.J., 2016. A Reactive Porous Flow Control on Mid-ocean Ridge
815 Magmatic Evolution. J. Petrol. 57, 2195–2220. https://doi.org/10.1093/petrology/egw074

Lissenberg, C.J., MacLeod, C.J., Howard, K.A., Godard, M., 2013. Pervasive reactive melt migration through fast-spreading lower oceanic crust (Hess Deep, equatorial Pacific Ocean). Earth Planet. Sci. Lett. 361, 436–447. https://doi.org/10.1016/j.epsl.2012.11.012

Longpre, M.-A., Klugel, A., Diehl, A., Stix, J., 2014. Mixing in mantle magma reservoirs prior to and during the 2011-2012 eruption at El Hierro, Canary Islands. Geology 42, 315–318. https://doi.org/10.1130/G35165.1

Lyons, J., Geist, D., Harpp, K., Diefenbach, B., Olin, P., Vervoort, J., 2007. Crustal growth by magmatic overplating in the Galápagos. Geology 35, 511. https://doi.org/10.1130/G23044A.1

Matzen, A.K., Baker, M.B., Beckett, J.R., Wood, B.J., Stolper, E.M., 2017a. The effect of liquid composition on the partitioning of Ni between olivine and silicate melt. Contrib. Mineral. Petrol. 172. https://doi.org/10.1007/s00410-016-1319-8

Matzen, A.K., Wood, B.J., Baker, M.B., Stolper, E.M., 2017b. The roles of pyroxenite and peridotite in the mantle sources of oceanic basalts. Nat. Geosci. 10, 530–535. https://doi.org/10.1038/ngeo2968

Meyer, P.S., Dick, H.J.B., Thompson, G., 1989. Cumulate gabbros from the Southwest Indian Ridge, 54S-7 16 E: implications for magmatic processes at a slow spreading ridge. Contrib. Mineral. Petrol. 103, 44–63. https://doi.org/10.1007/BF00371364

Mollo, S., Putirka, K., Misiti, V., Soligo, M., Scarlato, P., 2013. A new test for equilibrium based on clinopyroxene–melt pairs: Clues on the solidification temperatures of Etnean alkaline melts at post-eruptive conditions. Chem. Geol. 352, 92–100. https://doi.org/10.1016/j.chemgeo.2013.05.026

Naumann, T., Geist, D., 2000. Physical volcanology and structural development of Cerro Azul Volcano, Isabela Island, Galápagos: implications for the development of Galápagos-type shield volcanoes. Bull. Volcanol. 61, 497–514. https://doi.org/10.1007/s004450050001

Naumann, T.R., Geist, D.J., 1999. Generation of alkalic basalt by crystal fractionation of tholeiitic magma. Geology 27, 423. https://doi.org/10.1130/0091-7613(1999)027<0423:GOABBC>2.3.CO;2

Neave, D.A., Namur, O., Shorttle, O., Holtz, F., 2019. Magmatic evolution biases basaltic records of mantle chemistry towards melts from recycled sources. Earth Planet. Sci. Lett. 520, 199–211. https://doi.org/10.1016/j.epsl.2019.06.003

Neave, D.A., Putirka, K.D., 2017. A new clinopyroxene-liquid barometer, and implications for magma storage pressures under Icelandic rift zones. Am. Mineral. 102, 777–794. https://doi.org/10.2138/am-2017-5968

Park, J., Morgan, J.K., Zelt, C.A., Okubo, P.G., Peters, L., Benesh, N., 2007. Comparative velocity structure of active Hawaiian volcanoes from 3-D onshore–offshore seismic tomography. Earth Planet. Sci. Lett. 259, 500–516. https://doi.org/10.1016/j.epsl.2007.05.008

Peterson, M.E., Saal, A.E., Kurz, M.D., Hauri, E.H., Blusztajn, J.S., Harpp, K.S., Werner, R., Geist, D.J., 2017. Submarine Basaltic Glasses from the Galápagos Archipelago: Determining the Volatile Budget of the Mantle Plume. J. Petrol. 58, 1419–1450. https://doi.org/10.1093/petrology/egx059

Pietruszka, A.J., Heaton, D.E., Marske, J.P., Garcia, M.O., 2015. Two magma bodies beneath the summit of Kīlauea Volcano unveiled by isotopically distinct melt deliveries from the mantle. Earth Planet. Sci. Lett. 413, 90–100. https://doi.org/10.1016/j.epsl.2014.12.040

Poland, M.P., Miklius, A., Montgomery-Brown, E.K., 2015. Magma supply, storage, and transport at shield stage Hawaiian volcanoes, in: Characteristics of Hawaiian Volcanoes.

Poldervaart, A., Hess, H.H., 1951. Pyroxenes in the Crystallization of Basaltic Magma. J. Geol. 59, 472–489. https://doi.org/10.1086/625891

Putirka, K., 1999. Clinopyroxene + liquid equilibria to 100 kbar and 2450 K. Contrib. Mineral. Petrol. 135, 151–163. https://doi.org/10.1007/s004100050503

Putirka, K., 1997. Magma transport at Hawaii: Inferences based on igneous thermobarometry 4.

Putirka, K.D., 2008. Thermometers and Barometers for Volcanic Systems. Rev. Mineral. Geochem. 69, 61–120. https://doi.org/10.2138/rmg.2008.69.3

Roeder, P.L., Emslie, R.F., 1970. Olivine-liquid equilibrium. Contrib. Mineral. Petrol. 29, 275–289. https://doi.org/10.1007/BF00371276

870 Shejwalkar, A., Coogan, L.A., 2013. Experimental calibration of the roles of temperature and
871 composition in the Ca-in-olivine geothermometer at 0.1MPa. Lithos 177, 54–60.
872 https://doi.org/10.1016/j.lithos.2013.06.013
873 Sobolev, A.V., Hofmann, A.W., Kuzmin, D.V., Yaxley, G.M., Arndt, N.T., Chung, S.-L.,
874 Danyushevsky, L.V., Elliott, T., Frey, F.A., Garcia, M.O., Gurenko, A.A., Kamenetsky, V.S.,
875 Kerr, A.C., Krivolutskaya, N.A., Matvienkov, V.V., Nikogosian, I.K., Rocholl, A.,
876 Sigurdsson, I.A., Sushchevskaya, N.M., Teklay, M., 2007. The Amount of Recycled Crust in
877 Sources of Mantle-Derived Melts 316, 7.
878 Stock, M.J., Bagnardi, M., Neave, D.A., Maclennan, J., Bernard, B., Buisman, I., Gleeson, M.L.M.,
879 Geist, D., 2018. Integrated Petrological and Geophysical Constraints on Magma System
880 Architecture in the Western Galápagos Archipelago: Insights From Wolf Volcano. Geochem.
881 Geophys. Geosystems 19, 4722–4743. https://doi.org/10.1029/2018GC007936
882 Taracsák, Z., Hartley, M.E., Burgess, R., Edmonds, M., Iddon, F., Longpré, M.-A., 2019. High fluxes
883 of deep volatiles from ocean island volcanoes: Insights from El Hierro, Canary Islands.
884 Geochim. Cosmochim. Acta 258, 19–36. https://doi.org/10.1016/j.gca.2019.05.020
885 Thompson, R., 1987. Phase-equilibria constraints on the genesis and magmatic evolution of oceanic
886 basalts. Earth-Sci. Rev. 24, 161–210. https://doi.org/10.1016/0012-8252(87)90023-7
887 Thompson, R.N., Gibson, S.A., 2000. Transient high temperatures in mantle plume heads inferred
888 from magnesian olivines in Phanerozoic picrites. Nature 407, 502–506.
889 https://doi.org/10.1038/35035058
890 Vidito, C., Herzberg, C., Gazel, E., Geist, D., Harpp, K., 2013. Lithological structure of the Galápagos
891 Plume: Lithological Structure Galpagos Plume. Geochem. Geophys. Geosystems 14, 4214–
892 4240. https://doi.org/10.1002/ggge.20270
893 Vigouroux, N., Williams-Jones, G., Chadwick, W., Geist, D., Ruiz, A., Johnson, D., 2008. 4D gravity
894 changes associated with the 2005 eruption of Sierra Negra volcano, Galápagos.
895 GEOPHYSICS 73, WA29–WA35. https://doi.org/10.1190/1.2987399
896 Villagómez, D.R., Toomey, D.R., Geist, D.J., Hooft, E.E.E., Solomon, S.C., 2014. Mantle flow and
897 multistage melting beneath the Galápagos hotspot revealed by seismic imaging. Nat. Geosci.
898 7, 151–156. https://doi.org/10.1038/ngeo2062
899 Wager, L.R., Brown, G.M., Wadsworth, W.J., 1960. Types of Igneous Cumulates. J. Petrol. 1, 73–85.
900 https://doi.org/10.1093/petrology/1.1.73
901 Welsch, B., Hammer, J., Hellebrand, E., 2014. Phosphorus zoning reveals dendritic architecture of
902 olivine. Geology 42, 867–870. https://doi.org/10.1130/G35691.1
903 White, W.M., McBirney, A.R., Duncan, R.A., 1993. Petrology and geochemistry of the Galápagos
904 Islands: Portrait of a pathological mantle plume. J. Geophys. Res. Solid Earth 98, 19533–
905 19563. https://doi.org/10.1029/93JB02018
906 Wieser, P.E., Edmonds, M., Maclennan, J., Jenner, F.E., Kunz, B.E., 2019. Crystal scavenging from
907 mush piles recorded by melt inclusions. Nat. Commun. 10, 5797.
908 https://doi.org/10.1038/s41467-019-13518-2
909 Wieser, P.E., Edmonds, M., Maclennan, J., Wheeler, J., 2020. Microstructural constraints on
910 magmatic mushes under Kīlauea Volcano, Hawai‘i. Nat. Commun. 11, 14.
911 https://doi.org/10.1038/s41467-019-13635-y
912 Winpenny, B., Maclennan, J., 2011. A Partial Record of Mixing of Mantle Melts Preserved in
913 Icelandic Phenocrysts. J. Petrol. 52, 1791–1812. https://doi.org/10.1093/petrology/egr031
914 Wood, B.J., Blundy, J.D., 1997. A predictive model for rare earth element partitioning between
915 clinopyroxene and anhydrous silicate melt. Contrib. Mineral. Petrol. 129, 166–181.
916 https://doi.org/10.1007/s004100050330
917

918

FIGURES

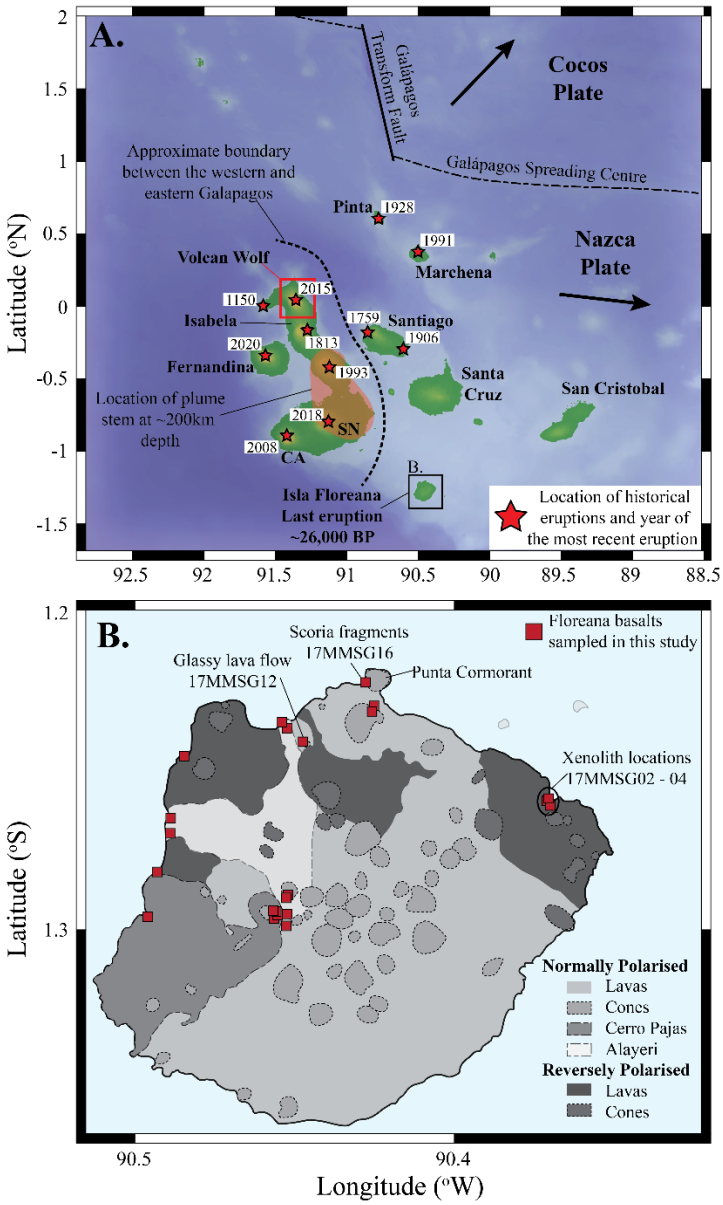

Figure 1 - A. Regional map of the Galápagos Archipelago highlighting the location of Isla Floreana, Cerro Azul (CA), Sierra Negra (SN) and Wolf volcanoes. Dates show the most recent eruptions at historically active volcanic centres. Black arrows show the direction of plate motion for the Nazca and Cocos tectonic plates, respectively. **B.** Geological map of Floreana adapted from Harpp et al. (2014a). Dashed lines delineate monogenetic scoria cones. Normally and reversely polarised lava flows are shown along with the largest (Cerro Pajas) and most recent (Alayeri; ~26,000 years) eruptions on Floreana.

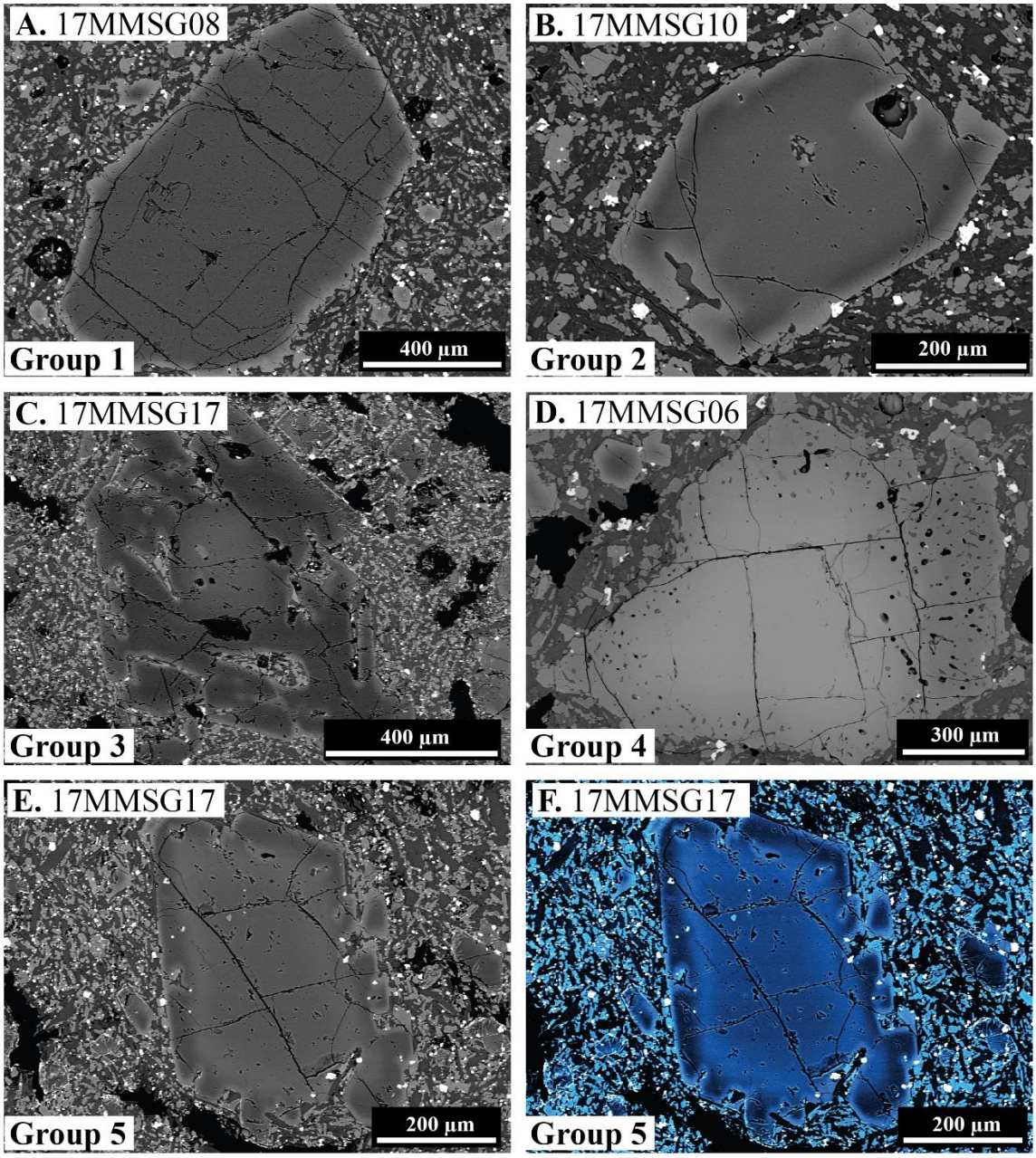

928

929 **Figure 2 -** SEM images of **A.** Group 1 olivines – euhedrual to subhedral crystal morphologies with
930 large, unzoned, crystal cores and narrow, normally-zoned rims. **B.** Group 2 olivines – subhedral to
931 euhedral crystals with clear, reverse-zoning profiles. **C.** Group 3 olivines – skeletal crystals with high
932 forsterite overgrowths on low forsterite cores. **D.** Group 4 olivines – anhedral crystals with sieved
933 textured, reverse zoned rims. **E.** (greyscale) and **F.** (false colour) Group 5 olivines – crystals preserve
934 at least 4 composition zones over ~100-200 µm.

935

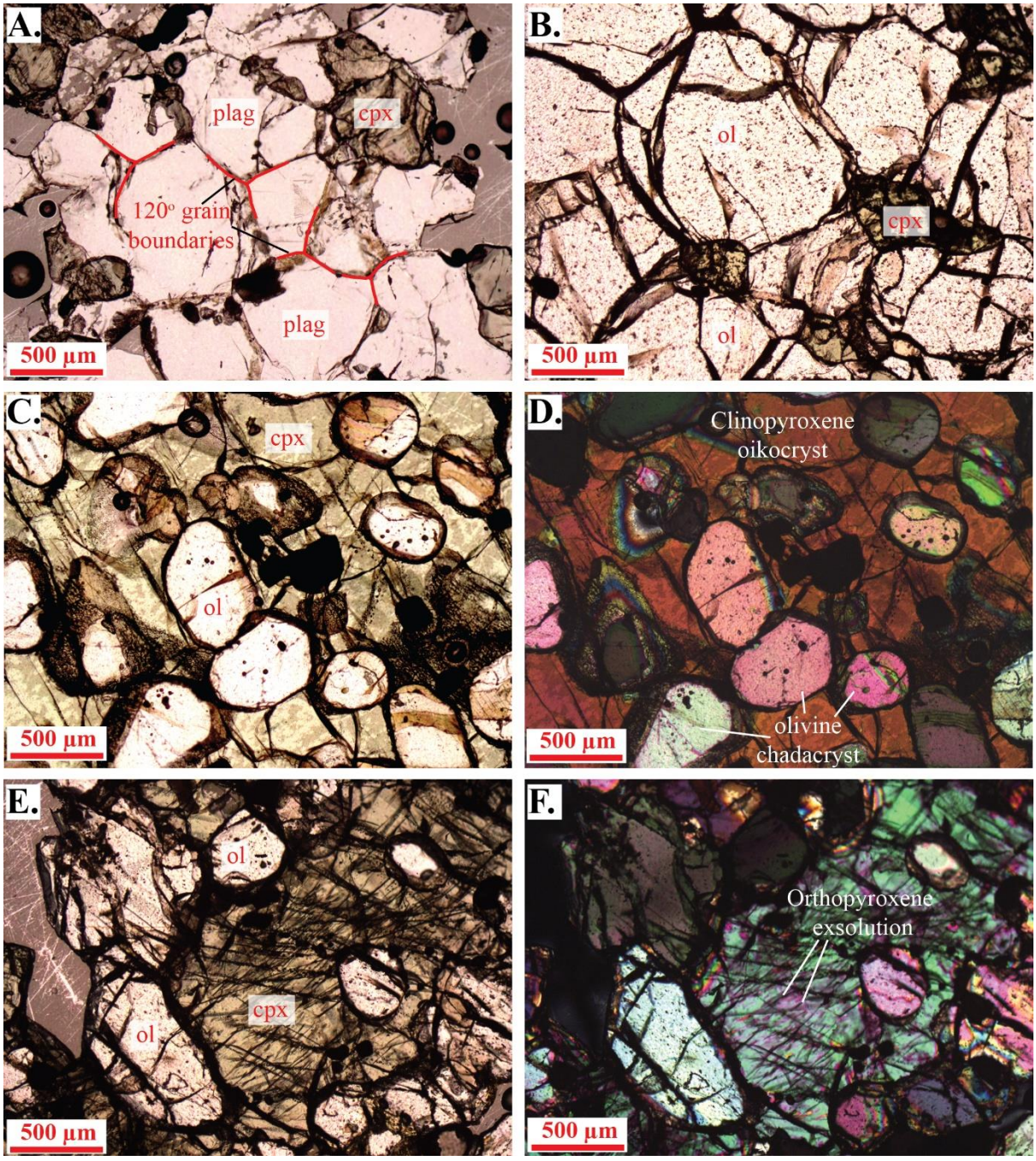

936

937 **Figure 3 -** Plane Polarised Light (**A. – C.** and **E.**) and Crossed Polarised Light (**D., F.**) images of
938 Floreana xenoliths. **A.** – gabbroic xenolith (17MMSG04b), highlighting near 120° grain boundaries at
939 monomineralic plagioclase (plag) triple junctions. **B.** – dunitic xenolith (17MMSG04c) with
940 intercumulus clinopyroxene growth. **C.** and **D.** – wehrlitic xenolith (17MMSG02c) showing a large
941 clinopyroxene (cpx) oikocryst surrounding olivine (ol) chadacrysts. **E.** and **F.** – wehrlitic xenolith
942 (sample 17MMSG03a) showing olivine chadacrysts within a clinopyroxene oikocryst. Orthopyroxene
943 exsolution lamallae are visible within the clinopyroxene.

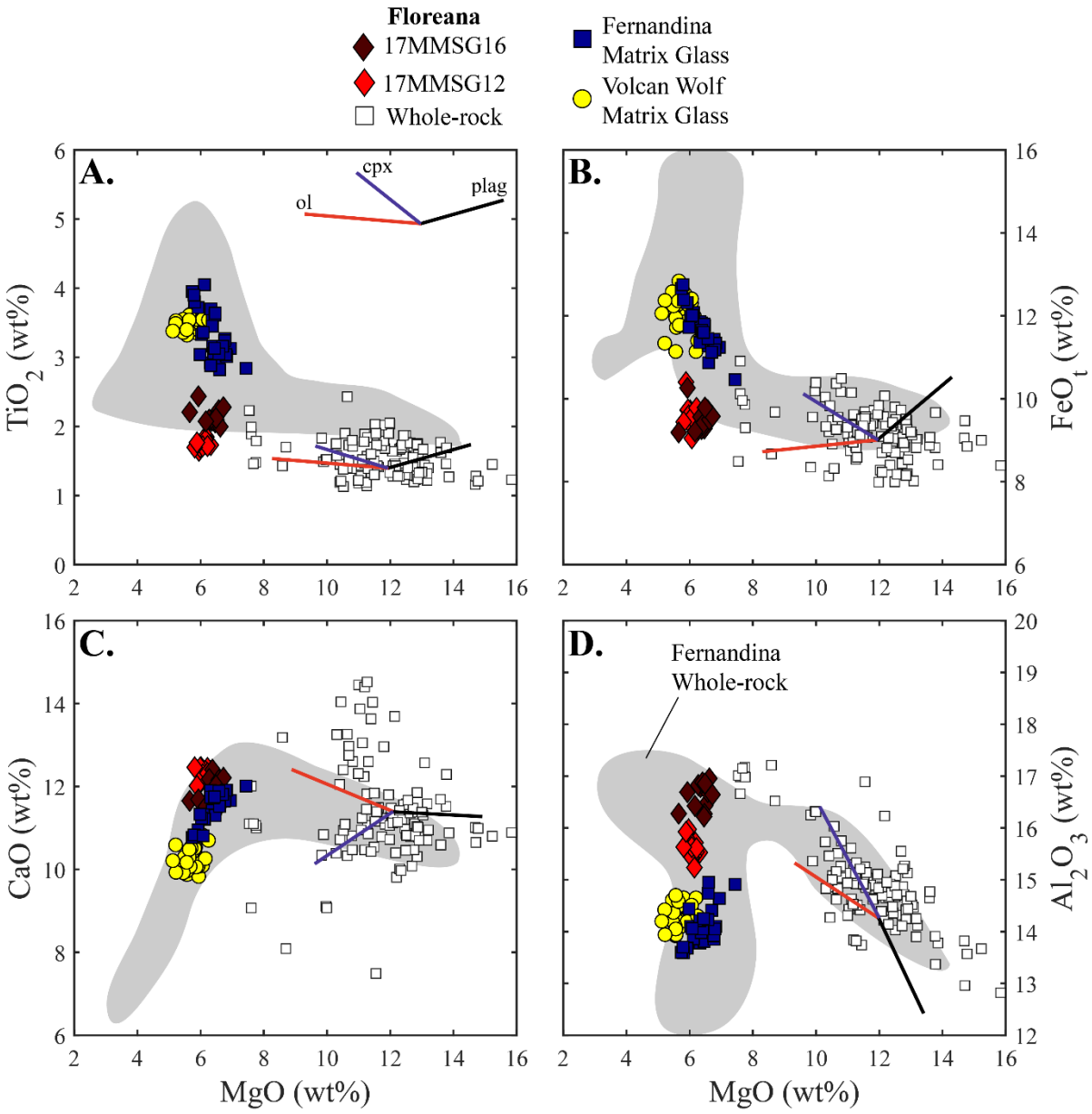

944

945 **Figure 4 –** Major element compositions of matrix glasses (this study) and whole-rocks (Harpp et al.,
946 2014a) from Floreana, as well as glasses from Fernandina (Peterson et al., 2017) and Wolf volcano
947 (Stock et al., 2018) in the western Galápagos Archipelago. Lines show trajectories of liquid
948 compositional evolution olivine (ol; red), clinopyroxene (cpx; blue) and plagioclase (plag; black)
949 crystallisation. The grey field shows whole-rock data from Isla Fernandina in the western Galápagos
950 (Allan and Simkin, 2000; Geist et al., 2006). The 2σ precision of our matrix glass analyses is smaller
951 than the symbol size.

952

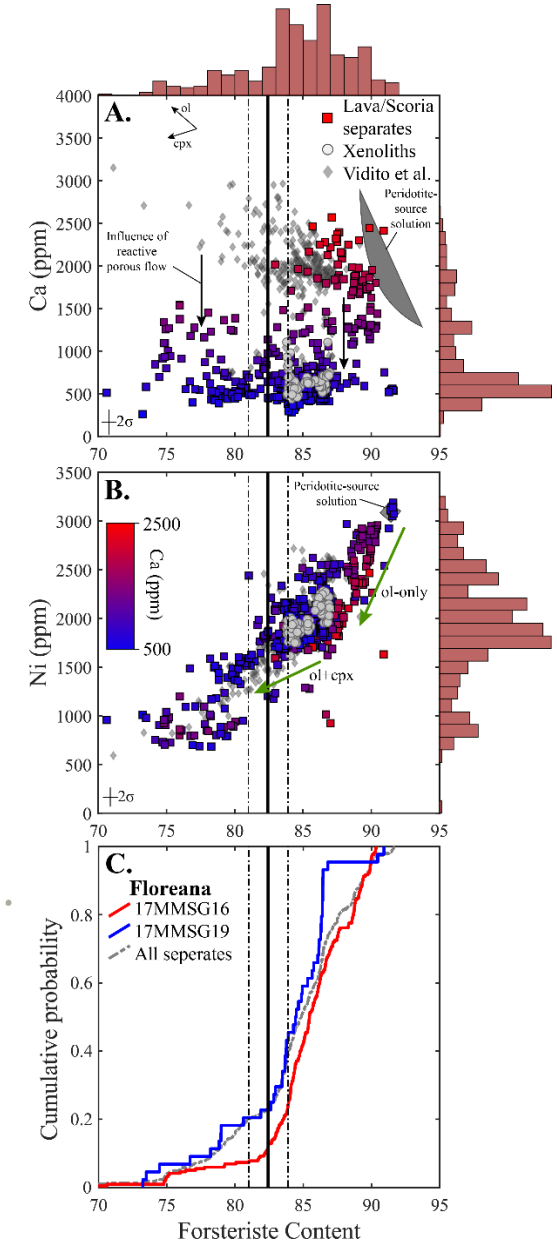

Figure 5 – Major and minor element compositions of olivine crystals from the Isla Floreana basalts. **A**. Fo vs. Ca and **B** Fo vs. Ni in Galápagos olivine crystals with analyses from our lava/scoria separates and xenolith samples, as well as a compilation of available olivine data from Floreana (Vidito et al. 2013). Our lava/scoria analyses are coloured according to their Ca concentration (see colour scale in **B**). The histograms above and to the right of the plots show the data distributions (excluding *in situ* analyses of xenolithic olivines). Peridotite source solutions are taken from Herzberg (2011) and Matzen et al. (2017a). Black arrows in **A.** show the trajectory of crystal compositional evolution during olivine (ol) and clinopyroxene (cpx) crystallisation (taken from Gleeson and Gibson, 2019) and the hypothesised influence of reactive porous flow. The green lines in **B.** show the trajectories of crystal compositional evolution during olivine only, followed by olivine + clinopyroxene fractional crystallisation (from Gleeson and Gibson, 2019). **C.** Cumulative probability of forsterite in olivine separates from our lava (17MMSG19) and scoria (17MMSG16) samples. A two-sample Kolmogorov-Smirnov test is used to assess the similarity of the forsterite distributions of the two samples (and all analyses from lava and scoria deposits in this study). Results indicate that the olivine populations from the two samples are drawn from the different distribution (p=0.0021). The vertical black lines show the forsterite compositions of crystals calculated to be in equilibrium with the matrix glass composition of tephra sample 17MMSG16 (K_d = 0.30±0.03 after Roeder and Emslie, 1970).

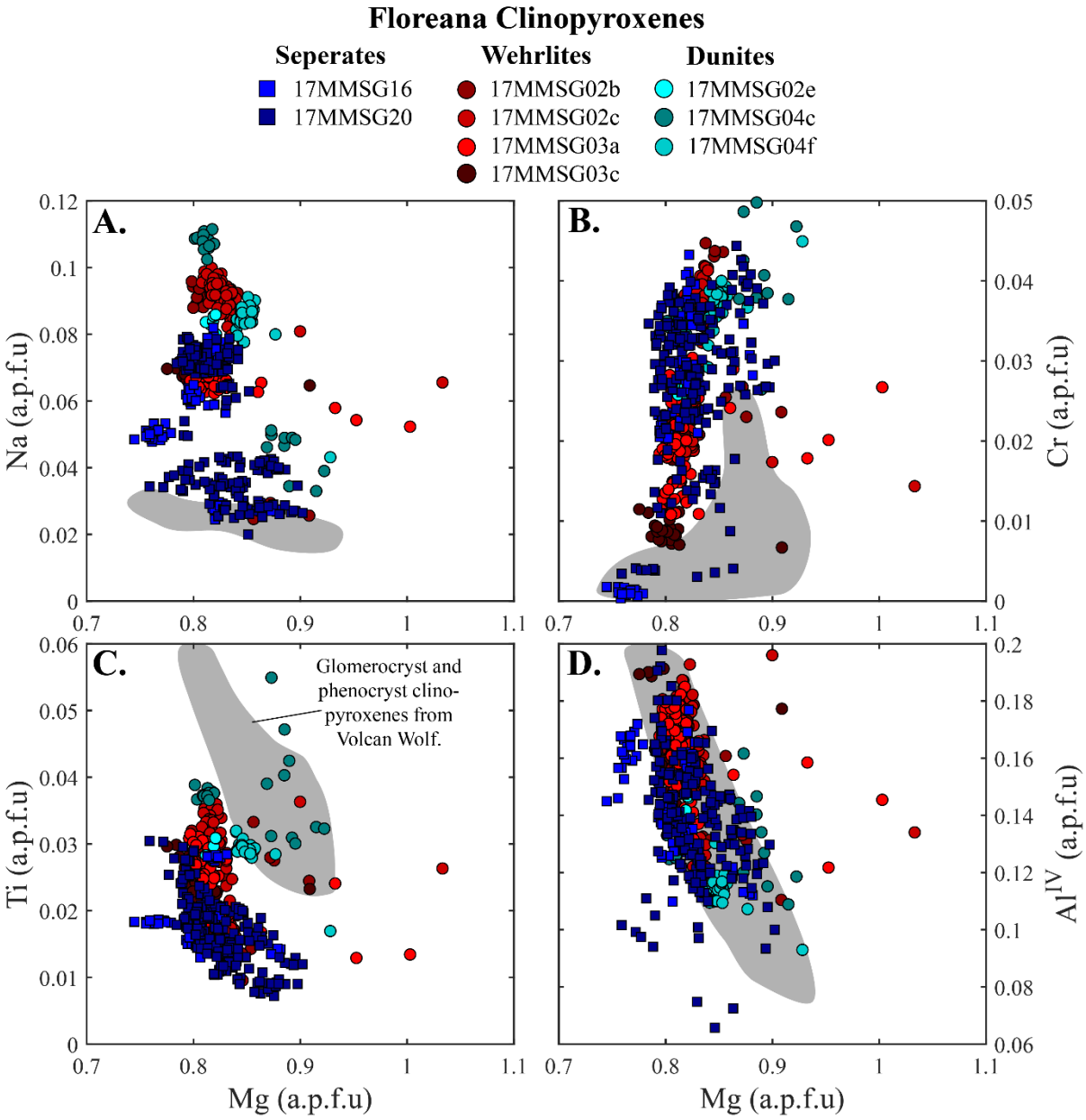

980

981 **Figure 6** – Major element composition of Floreana clinopyroxenes from our scoria samples and
982 wehrlite and dunite xenoliths. The grey field shows the compositions of clinopyroxenes from Wolf
983 volcano in the western Galápagos Archipelago (from Stock et al. 2018). The 2σ precision of our
984 clinopyroxene analyses is smaller than the symbol size.

985

986

987

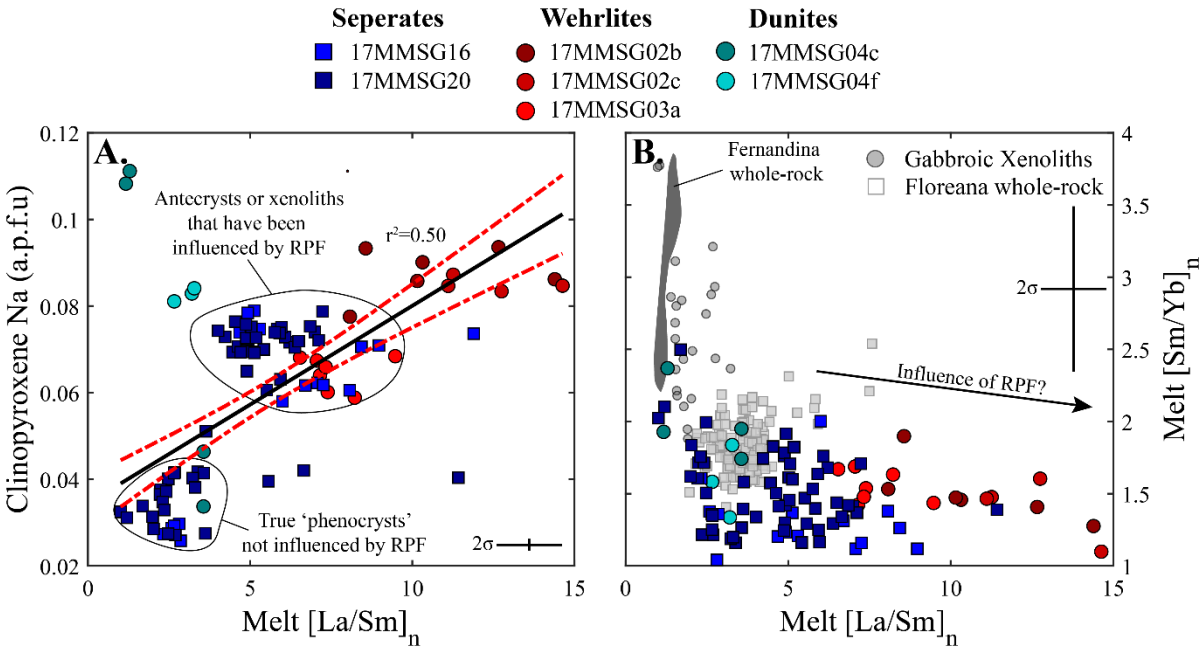

988

989 **Figure 7 – A.** $[La/Sm]_n$ vs. Na in clinopyroxenes from our scoria samples and wehrlite and dunite
990 xenoliths. The black line shows a regression through the data ($r^2 = 0.50$) and the red dashed lines
991 show the 95% confidence limits on the regression. **B.** $[La/Sm]_n$ vs. $[Sm/Yb]_n$ of melts calculated to be
992 in equilibrium with our Floreana clinopyroxenes using the model of Wood and Blundy (1997). The
993 black arrow shows the approximate trend of crystal compositional evolution hypothesised to occur as
994 a result of reactive porous flow. The grey field shows whole-rock compositions from Fernandina
995 (Geist et al., 2006; White et al., 1993). **B** additionally shows the whole-rock compositions of erupted
996 Floreana lavas (Harpp et al., 2014a) and analyses of the gabbroic xenoliths from Floreana (this study).
997 Error bars show the fully propagated 2σ precision of our analyses.

998

999

1000

1001

1002

1003

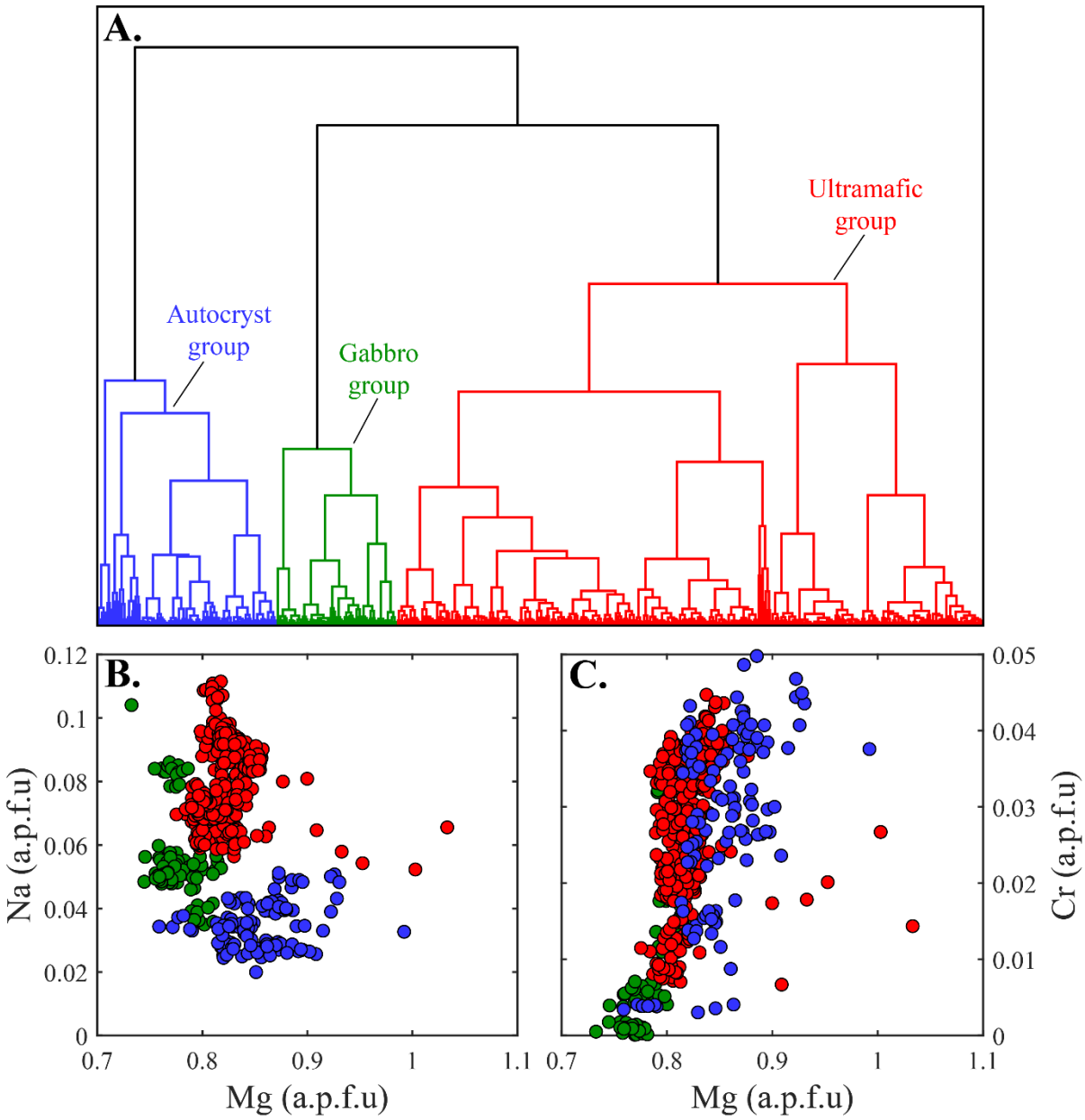

Figure 8 – A. Hierarchical cluster analysis of our clinopyroxene major element analyses. Colours show the high-level division of crystal compositions into three groups: Group 1 is predominantly comprised of crystals from wehrlite and dunite xenoliths (red), Group 2 is predominantly comprised of crystals from gabbroic xenoliths (green) and Group 3 (blue) is dominated by crystals separated from scoria samples. **B** Na vs Mg and **C** Cr vs Mg in our clinopyroxene analyses from the scoria and xenoliths, coloured by their group.

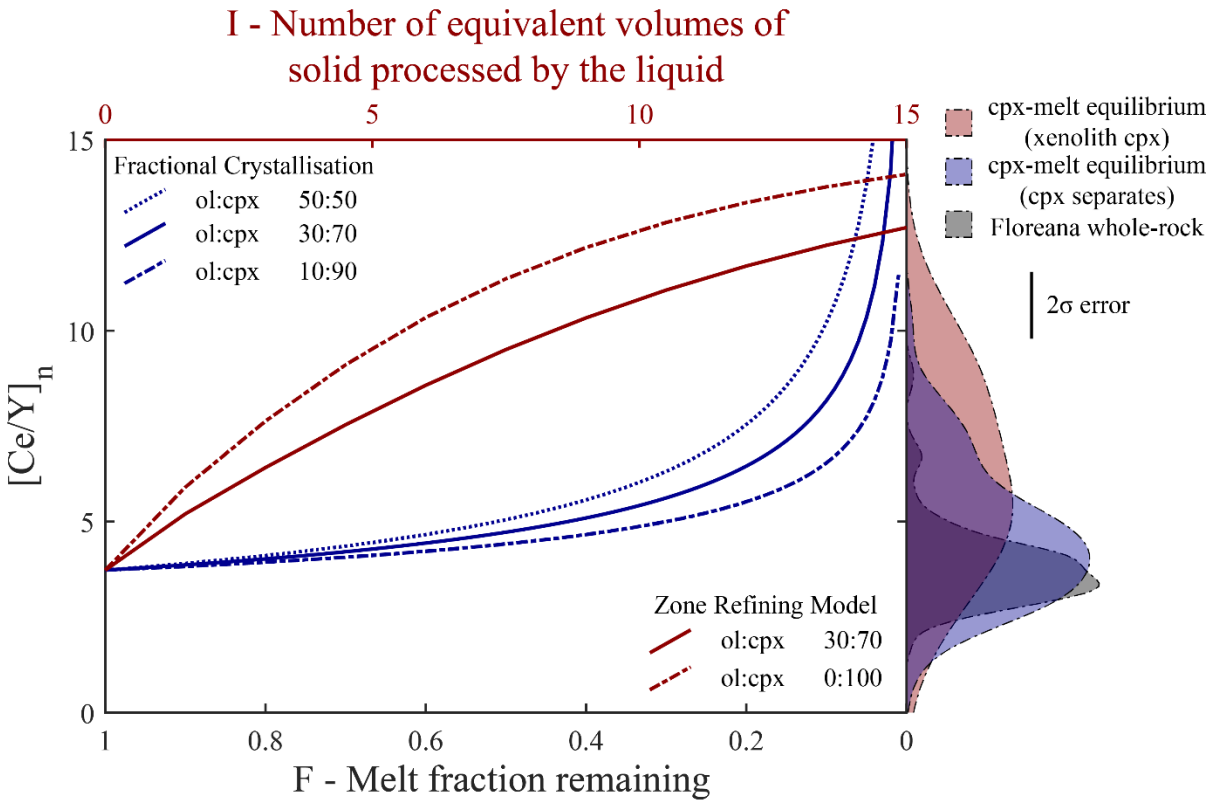

Figure 9 – Models showing the evolution of melt $[Ce/Y]_n$ ratios as a function of the melt fraction remaining (F) during fractional crystallisation and as a function of the number of equivalent volumes of solid processed by the liquid (I) during reactive porous flow (red; using the zone-refining model of Harris, 1957). Line types show how models vary with different ratios of crystallising olivine (ol) and clinopyroxene (cpx). The kernel density plots to the right show the $[Ce/Y]_n$ density distributions of liquids calculated to be in equilibrium with clinopyroxene crystals in our wehrlite and dunite xenoliths (red), scoria samples (blue; 2σ error for the clinopyroxene analyses is shown by the black bar), and whole-rock analyses of erupted Floreana basalts (grey; Harpp et al., 2014a). Partition coefficients were calculated for clinopyroxene using the method of Wood and Blundy (1997), the mean major element composition of the group 3 clinopyroxenes from this study, a temperature of 1225ºC, and a pressure of 700 MPa. Initial Ce and Y concentrations for both models were taken as the mean values from the whole-rock dataset of Harpp et al. (2014a). Calculation increments are 0.01 in F and 0.1 in I.

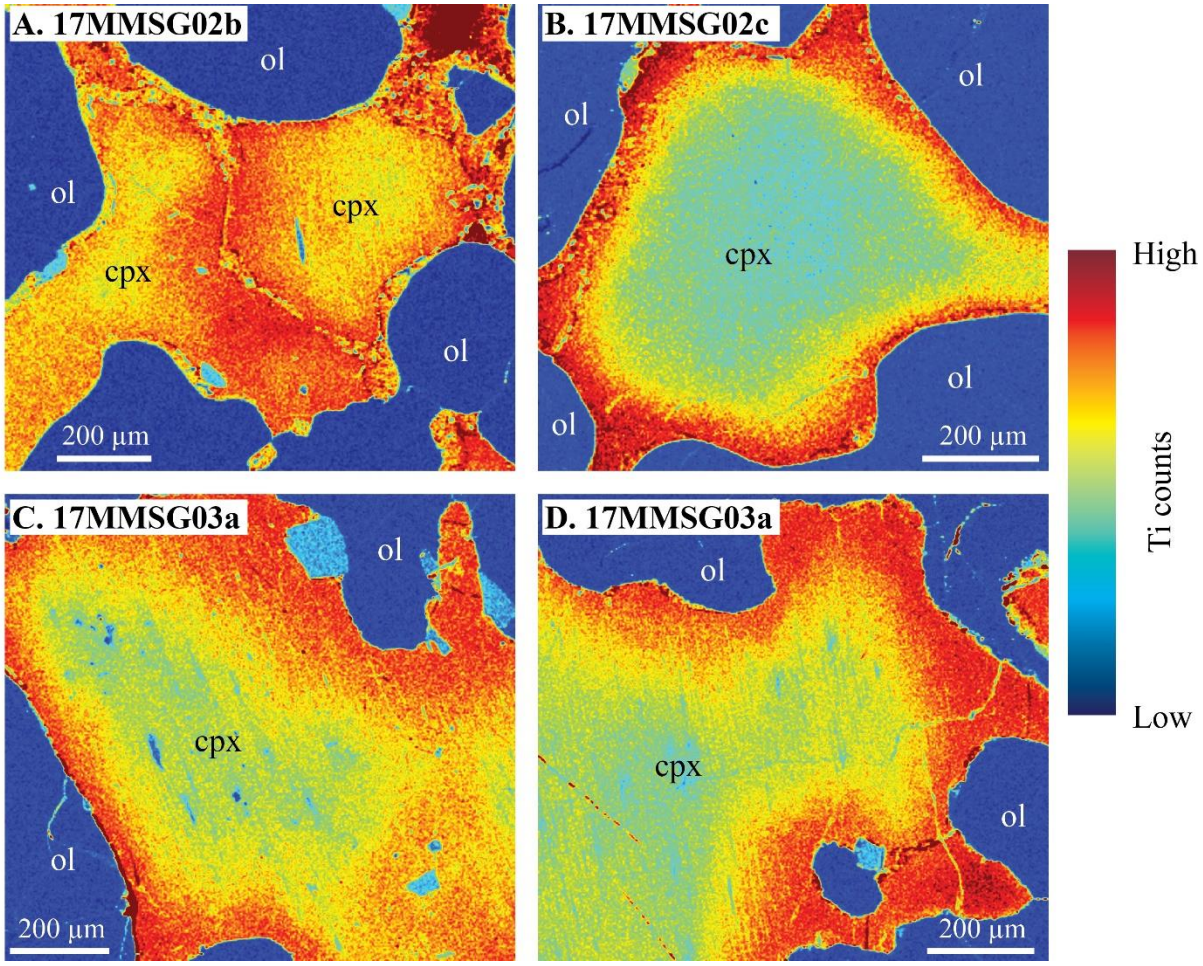

Figure 10 – Ti maps of key clinopyroxene crystals in the Floreana wehrlite xenoliths. These maps display clear zoning in the xenolithic clinopyroxenes with Ti-poor cores and Ti-rich rims. The dark blue regions surrounding clinopyroxene grains are olivine crystals.

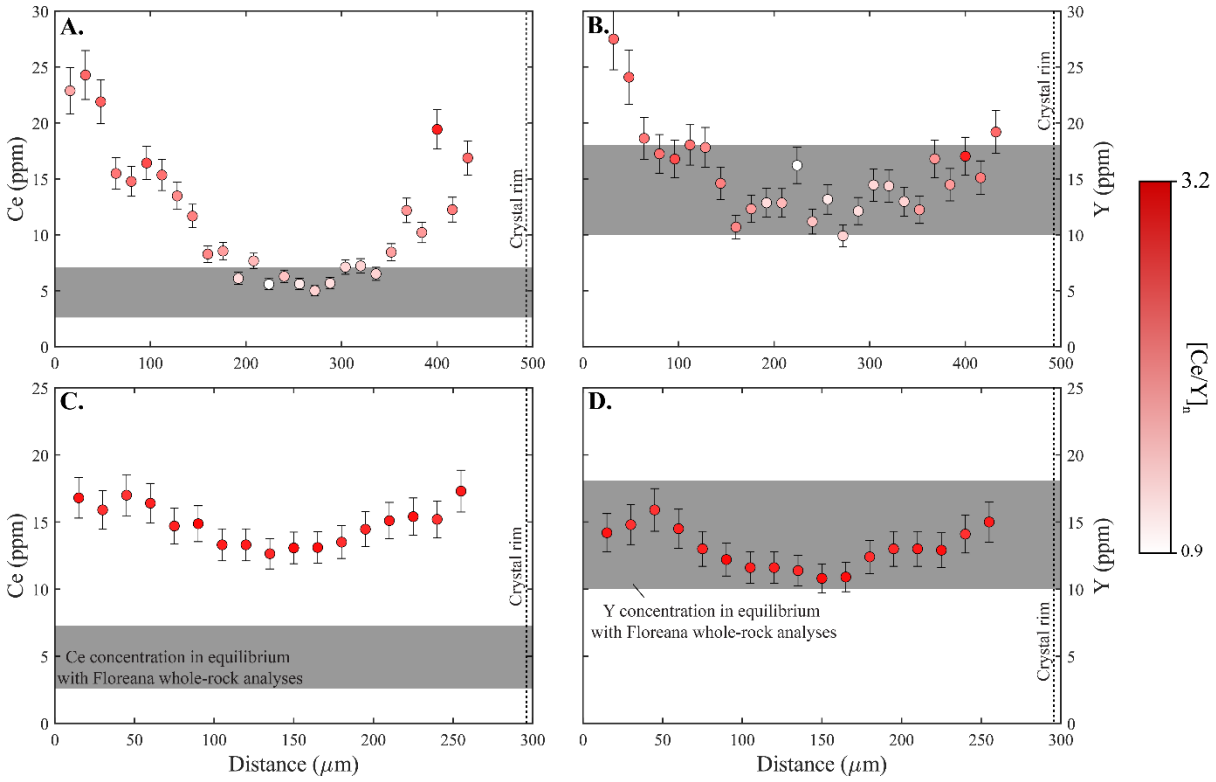

Figure 11 – LA-ICP-MS transects showing Ce (**A, C**) and Y (**B, D**) zoning across two clinopyroxene grains in a wehrlitic xenolith (17MMSG02c). **A.** and **B.** show a transect across the core of a large clinopyroxene oikocryst. **C.** and **D.** show a transect across the apparent core of a smaller clinopyroxene oikocryst. Points are coloured according to their $[Ce/Y]_n$ ratio (see colour scale). The grey bars show the crystal compositions calculated to be in equilibrium with whole-rock analyses of erupted Floreana basalts (Harpp et al., 2014a).

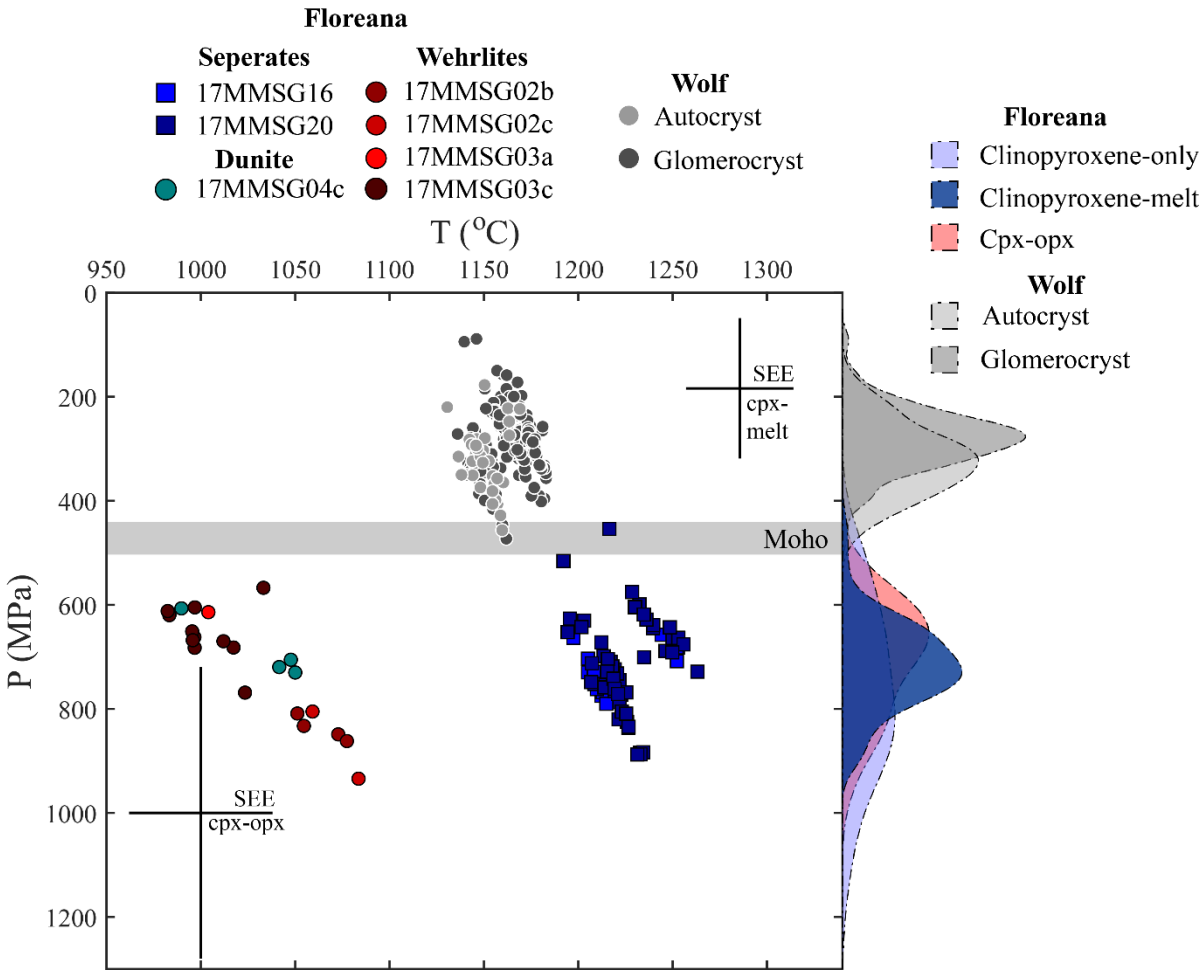

Figure 12 – Petrological thermobarometry results. The kernel density plots to the right show the density distributions of barometric results from different models (light blue – clinopyroxene-only, Putirka (2008); dark blue – clinopyroxene-melt, Neave and Putirka (2017); red – clinopyroxene-orthopyroxene Putirka (2008)). The grey bar shows the Moho depth beneath Fernandina (from Feighner and Richards, 1994) and the grey points and kernel density estimates show clinopyroxene-melt thermobarometric results for autocrysts and glomerocrysts from Wolf volcano for comparison (from Stock et al., 2018).

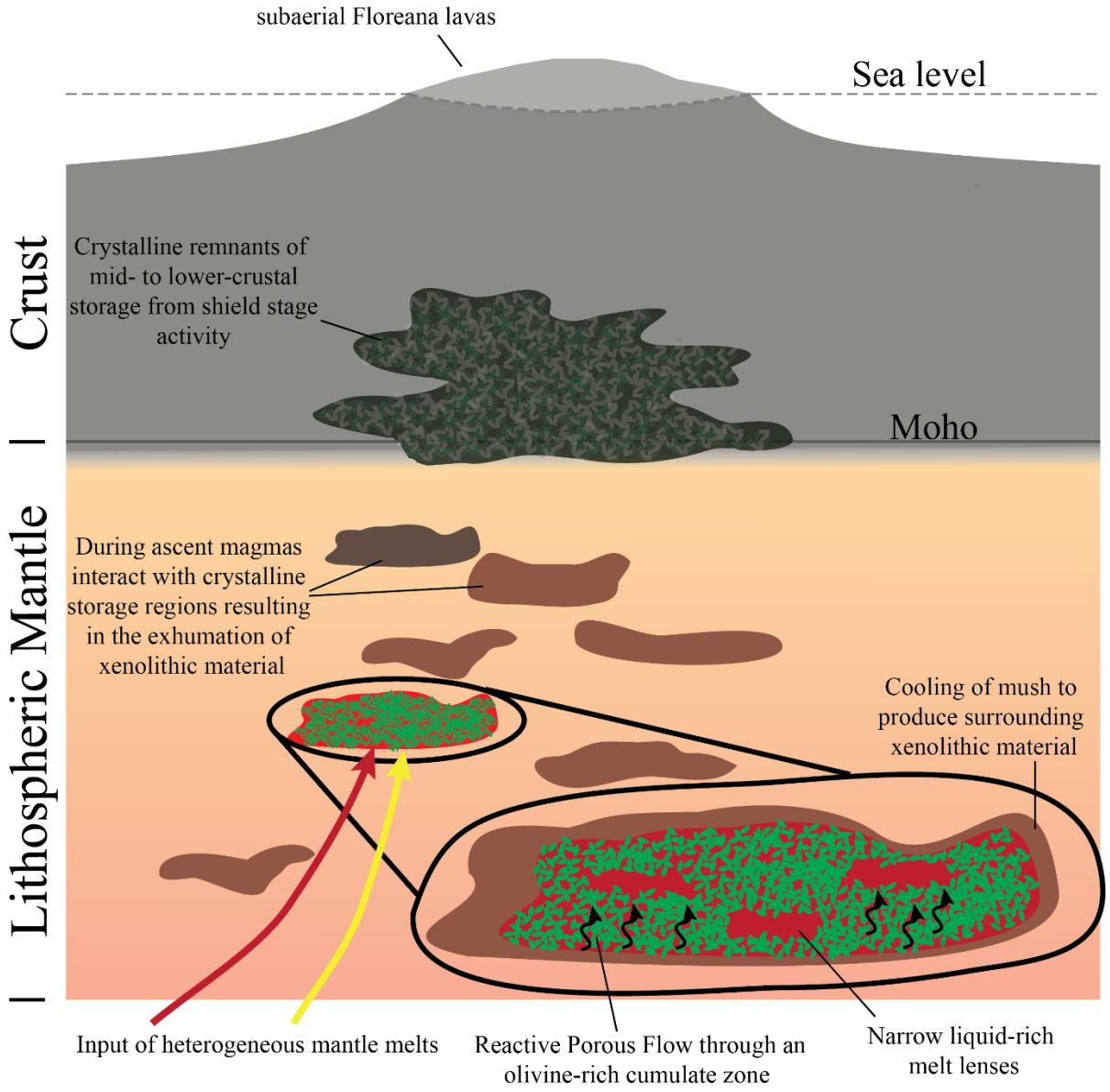

1065

1066 **Figure 13** – Schematic illustration of the magma plumbing system beneath Floreana. No magma
1067 storage is identified within the crust. Instead, our barometric results indicate that Floreana magmas
1068 ascend directly from the upper mantle, where they are stored at a depth of ~23.7 ±5.1 km. Floreana
1069 magma storage regions are dominated by crystal-rich domains (i.e. mush). Reactive porous flow is
1070 identified as an important mechanism of melt migration and magma differentiation in the crystal-rich
1071 storage regions, although our results shows that some crystallisation occurs within liquid-rich
1072 domains.

1073

1074

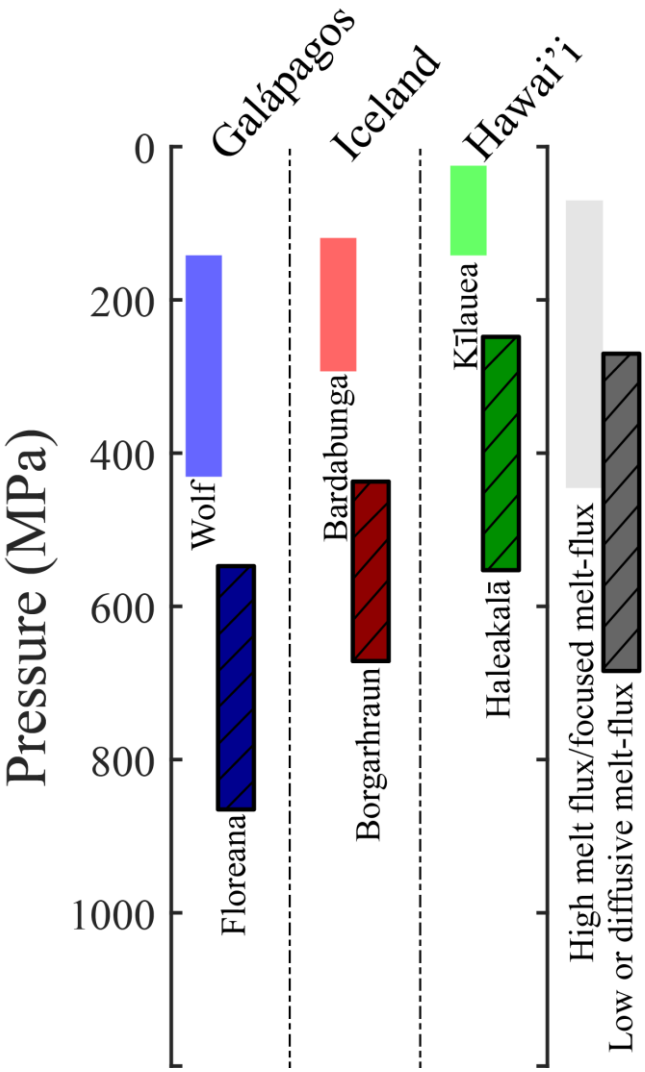

Figure 14 - Compilation of barometric estimates from different hotspot localities. Boxes without boarders show magma storage pressures at central volcanic systems, proximal to the centre of high buoyancy plumes (i.e. those with a high flux of mantle-derived magma), and boxes with black boarders and dashes show magma storage pressures at volcanic systems that are off-axis (i.e. those with a low flux of mantle-derived magma). The pressure of magma storage is greater in regions of Hawai'i, Iceland, and the Galápagos that are characterised by a relatively low flux of mantle-derived magma. Barometric estimates are taken from: Poland et al. (2015) for Kīlauea, using multiple available data streams to create a model of summit magma storage (~25-150 MPa); Hammer et al. (2016) for Haleakalā using clinopyroxene melt barometry (~400 ±160 MPa); Hartley et al. (2018) for Bardabunga using OPAM (210 ±70 MPa); Neave and Putirka (2017) for Borgarhraun using clinopyroxene-melt barometry (570 ±120 MPa); Stock et al. (2018) for Volcan Wolf using OPAM and clinopyroxene-melt barometry (280 ±140 MPa; OPAM results), and this study for Floreana using clinopyroxene-melt barometry (717 ±165 MPa).